

Robustness of cosmic birefringence measurement against Galactic foreground emission and instrumental systematics

P. Diego-Palazuelos^{1,2} E. Martínez-González,¹ P. Vielva,¹ R. B. Barreiro,¹ M. Tristram,³ E. de la Hoz,^{1,2} J. R. Eskilt,⁴ Y. Minami,⁵ R. M. Sullivan,⁶ A. J. Banday,⁷ K. M. Górski,^{8,9} R. Keskitalo,^{10,11} E. Komatsu,^{12,13} and D. Scott⁶

¹Instituto de Física de Cantabria (CSIC - Universidad de Cantabria), Avenida los Castros s/n, 39005 Santander, Spain

²Departamento de Física Moderna, Universidad de Cantabria, Avenida de los Castros s/n, 39005 Santander, Spain

³Université Paris-Saclay, CNRS/IN2P3, IJCLab, 91405 Orsay, France

⁴Institute of Theoretical Astrophysics, University of Oslo, Blindern, N-0315 Oslo, Norway

⁵Research Center for Nuclear Physics, Osaka University, Ibaraki, Osaka 567-0047, Japan

⁶Department of Physics & Astronomy, University of British Columbia, 6224 Agricultural Road, Vancouver, British Columbia, Canada

⁷IRAP, Université de Toulouse, CNRS, CNES, UPS, Toulouse, France

⁸Jet Propulsion Laboratory, California Institute of Technology, 4800 Oak Grove Drive, Pasadena, California, USA

⁹Warsaw University Observatory, Aleje Ujazdowskie 4, 00-478 Warszawa, Poland

¹⁰Computational Cosmology Center, Lawrence Berkeley National Laboratory, Berkeley, California 94720, USA

¹¹Space Sciences Laboratory, University of California, Berkeley, California 94720, USA

¹²Max Planck Institute for Astrophysics, Karl-Schwarzschild-Strasse 1, D-85748 Garching, Germany

¹³Kavli Institute for the Physics and Mathematics of the Universe (Kavli IPMU, WPI), Today Institutes for Advanced Study, The University of Tokyo, Kashiwa 277-8583, Japan

E-mail: diegop@ifca.unican.es

Abstract. The polarization of the cosmic microwave background (CMB) can be used to search for parity-violating processes like that predicted by a Chern-Simons coupling to a light pseudoscalar field. Such an interaction rotates E modes into B modes in the observed CMB signal by an effect known as cosmic birefringence. Even though isotropic birefringence can be confused with the rotation produced by a miscalibration of the detectors' polarization angles the degeneracy between both effects is broken when Galactic foreground emission is used as a calibrator. In this work, we use realistic simulations of the High-Frequency Instrument of the *Planck* mission to test the impact that Galactic foreground emission and instrumental systematics have on the recent birefringence measurements obtained through this technique. Our results demonstrate the robustness of the methodology against the miscalibration of polarization angles and other systematic effects, like intensity-to-polarization leakage, beam leakage, or cross-polarization effects. However, our estimator is sensitive to the EB correlation of polarized foreground emission. Here we propose to correct the bias induced by dust EB by modeling the foreground signal with templates produced in Bayesian component-separation analyses that fit parametric models to CMB data. Acknowledging the limitations of currently available dust templates like that of the **Commander** sky model, high-precision CMB data and a characterization of dust beyond the modified blackbody paradigm are needed to obtain a definitive measurement of cosmic birefringence in the future.

Contents

1	Introduction	1
2	Methodology	4
3	NPIPE simulations and Galactic masks	8
4	Impact of Galactic foregrounds	10
5	Impact of instrumental systematics	15
6	Impact of noise bias	20
7	Conclusions	22
A	Cross-spectra estimator	23
B	Comparison with MCMC sampling	27
C	Calculation of the covariance matrix	29
D	Modeling Galactic foregrounds in the covariance matrix	30

1 Introduction

Parity-violating processes are predicted by several extensions of the standard model of cosmology and particle physics [1]. For example, axion-like particles [2] and other dark energy and dark matter models [3, 4] introduce a new parity-violating pseudoscalar field, ϕ , that can couple to the electromagnetic tensor through a Chern-Simons interaction [5–7]. Such an interaction makes the phase velocities of the right- and left-handed helicity states of photons differ, rotating the plane of linear polarization clockwise on the sky by an angle $\beta = -\frac{1}{2}g_{\phi\gamma} \int \frac{\partial\phi}{\partial t} dt$ that depends on the coupling constant of the pseudoscalar field to photons $g_{\phi\gamma}$, and the time evolution of the field. This rotation is what we call “cosmic birefringence” because it is as if space itself acted like a birefringent material (see Ref. [8] for a review). Cosmic birefringence can also be produced by the Faraday rotation originating from primordial magnetic fields [9, 10]. Unlike the Chern-Simons interaction, Faraday rotation does depend on the photon energy, leading to a $\beta \propto \nu^{-2}$ birefringence angle. A frequency-dependent birefringence is also predicted by superluminal Lorentz-violating electrodynamics emerging from a non-vanishing Weyl tensor ($\beta \propto \nu$) [11], and some quantum gravity models that modify the dispersion relation of photons ($\beta \propto \nu^2$) [12]. Nevertheless, in this work, we focus on the frequency-independent birefringence predicted by light pseudoscalar fields, since the analysis of *Planck* data presented in Ref. [13] highly disfavored these other theories.

Although we know that birefringence must be a small effect, in principle we could constrain β by measuring the rotation of the plane of polarization of a well-known source of linearly polarized light situated at a far enough distance to allow photons to accumulate a

significant rotation. Emitted at the epoch of recombination and with its polarization angular power spectra accurately predicted by the Λ cold dark matter (Λ CDM) model, the cosmic microwave background (CMB) is, therefore, the ideal tool in the search for cosmic birefringence [14].

We can model the effect of a constant, isotropic, and frequency-independent birefringence angle (like the one that a homogeneous axion-like field of mass $10^{-33}\text{eV} \leq m_\phi \leq 10^{-28}\text{eV}$ might produce [13, 15, 16]) as a rotation of the plane of linear polarization of CMB photons. In this way, the spherical harmonic coefficients of the E and B modes of the CMB polarization that we observe (“o” superscript) would be a rotation of those emitted at recombination:

$$\begin{pmatrix} E_{\ell m}^o \\ B_{\ell m}^o \end{pmatrix} = \begin{pmatrix} c(2\beta) & -s(2\beta) \\ s(2\beta) & c(2\beta) \end{pmatrix} \begin{pmatrix} E_{\ell m}^{\text{CMB}} \\ B_{\ell m}^{\text{CMB}} \end{pmatrix}. \quad (1.1)$$

For brevity, throughout this work we refer to the sine, cosine, and tangent functions as “s”, “c”, and “t”, respectively. Under this approximation, and without solving the Boltzmann equations coupled to the light pseudoscalar field (as done, e.g., in Ref. [16]), we can model the observed angular power spectra as a rotation of the CMB spectra predicted in Λ CDM:

$$\begin{pmatrix} C_\ell^{EE,o} \\ C_\ell^{EB,o} \\ C_\ell^{BB,o} \end{pmatrix} = \begin{pmatrix} c^2(2\beta) & -s(4\beta) & s^2(2\beta) \\ \frac{1}{2}s(4\beta) & c(4\beta) & -\frac{1}{2}s(4\beta) \\ s^2(2\beta) & s(4\beta) & c^2(2\beta) \end{pmatrix} \begin{pmatrix} C_\ell^{EE,\Lambda\text{CDM}} \\ 0 \\ C_\ell^{BB,\Lambda\text{CDM}} \end{pmatrix}. \quad (1.2)$$

From Eq. (1.2) it follows that the observed EB correlation can be written as a rotation of the observed EE and BB angular power spectra like

$$C_\ell^{EB,o} = \frac{t(4\beta)}{2} (C_\ell^{EE,o} - C_\ell^{BB,o}). \quad (1.3)$$

Eq. (1.3) has been the basis for the majority of the harmonic-space methodologies applied in the past to measure cosmic birefringence from CMB polarization data [17–24]. However, those analyses have often been dominated by systematic uncertainties. In particular, the miscalibration of the detector’s polarization angle is one of the most pernicious systematics for this type of analysis, since it produces a rotation of the observed polarization signal that is degenerate with that of birefringence [25–28]. Namely, for an α miscalibration angle, the CMB spherical harmonic coefficients in Eq. (1.1) would be rotated by $\beta + \alpha$, so that the observed EB correlation in Eq. (1.3) yields $\beta + \alpha$ instead of β . In this way, the calibration strategies used for currently available CMB datasets tend to limit the systematic uncertainty attainable through the analysis of EB to 0.5° – 1° [20, 29–33]. In addition to the miscalibration of polarization angles, other systematic effects, like intensity-to-polarization leakage, beam leakage, or cross-polarization effects, also produce spurious EB correlations that contribute to the total systematic uncertainty [25–28]. Although the accuracy in the calibration of polarization angles is expected to improve in the near future [34–38], systematics will play an even more critical role in the precision measurements of CMB polarization envisioned for next-generation experiments [39–41].

To overcome the limitation imposed by the calibration of polarization angles, Refs. [42–44] proposed a novel methodology to simultaneously determine birefringence and miscalibration angles through the use of polarized Galactic foreground emission. Foreground emission can be used to break the degeneracy between the α and β angles since Galactic foreground photons are negligibly affected by cosmic birefringence due to their small propagation length.

That methodology has proven to successfully capture polarization angle miscalibrations and provide robust birefringence measurements [42–45]. Ref. [46] applied it to polarization data from the *Planck* mission High-Frequency Instrument (HFI) third public release (PR3) [47] and obtained a birefringence measurement of $\beta = 0.35^\circ \pm 0.14^\circ$ (68% C.L.), with no apparent contribution from systematic uncertainties.

The subsequent study of HFI data from *Planck*'s fourth public release (known as PR4 or NPIPE reprocessing) [48] done in Ref. [49] yielded a birefringence angle of $\beta = 0.30^\circ \pm 0.11^\circ$ (68% C.L.). More importantly, that study revealed that, although robust against systematics, the methodology is sensitive to the *EB* correlation inherent in polarized foreground emission. The contribution from a possible foreground *EB* correlation had been considered but ultimately neglected in previous works [42–44, 46], since the *EB* correlation of both Galactic synchrotron and dust emissions is still statistically compatible with zero according to current experimental constraints [50, 51].

Nevertheless, the misalignment between the filamentary dust structures of the interstellar medium and the plane-of-sky orientation of the Galactic magnetic field is expected to induce a non-null *EB* correlation on Galactic dust emission that can bias the measurement of birefringence [52–54]. Two independent approaches to model dust *EB* and correct for such a bias were proposed in Ref. [49]: one based on the *EB* correlation predicted from the misalignment of dust filaments and magnetic field lines [53]; and another one that takes the *EB* from the foreground templates produced by Bayesian component-separation analyses that fit parametric models to CMB data such as the **Commander**¹ sky model [55–58].

Produced by a different physics, no alignment mechanism is known to induce a non-null *EB* correlation in synchrotron radiation. The study of the synchrotron-dominated frequencies of WMAP and the Low-Frequency Instrument (LFI) of *Planck* in Refs. [13, 51, 59] suggests that such a hypothetical synchrotron *EB* has little effect on the measurement of birefringence. Correcting only for dust *EB*, the combined analysis of *Planck* HFI and LFI with WMAP data gave a birefringence angle of $\beta = 0.342^\circ_{-0.091^\circ}^{+0.094^\circ}$ (68% C.L.) [59].

The aim of this work is to test the robustness of these cosmic birefringence measurements against Galactic foreground emission and instrumental systematics using high-fidelity simulations of *Planck* data. Such an analysis was part of the study on the impact of systematics undertaken in Ref. [49], but finally not described in that publication due to space limitations. Although the results presented here are restricted to simulations of *Planck* HFI, our conclusions on the impact of dust *EB* and the robustness of the methodology against instrumental systematics are expected to extend to the other measurements presented above.

The original implementation of the methodology presented in Refs. [42–44] relies on Markov chain Monte Carlo (MCMC) methods to sample the likelihood and obtain the posterior distribution. To reduce the computational cost of that approach, in this work, we present an iterative algorithm based on the small-angle approximation to semi-analytically calculate the maximum likelihood solution. With this implementation we achieve a great reduction of execution time without compromising accuracy and precision, making the algorithm ideal for simulation-based studies of different experimental configurations, foreground models, or systematic effects. This method is the extension to the simultaneous determination of both cosmic birefringence and miscalibrated polarization angles of the methodology originally presented in Ref. [60].

¹**Commander** products are available at <https://pla.esac.esa.int/#maps>, and the code itself at <https://github.com/Cosmoglob/Commander>.

This work is structured as follows. In section 2, we present our methodology for the simultaneous estimation of birefringence and miscalibration angles. To test and validate our algorithm in a realistic scenario, we use the official end-to-end simulations provided in the NPIPE data release [48] to build the two simulation sets described in section 3. The effect that Galactic foregrounds, instrumental systematics, and instrumental noise bias have on our estimates are considered in sections 4, 5, and 6, respectively. Final comments and conclusions are left for section 7. Some technical aspects regarding the more general formulation of the estimator in terms of frequency cross-spectra, the comparison with the standard MCMC implementation, the calculation of the covariance matrix, and the modeling of Galactic foregrounds in the covariance matrix, are presented in appendices A, B, C, and D, respectively.

2 Methodology

Both the isotropic birefringence angle β and the α_i miscalibration of polarization angles rotate the polarization signal observed by CMB experiments at any given frequency band ν_i . However, the amplitude of the birefringence rotation depends on the difference between the value of the pseudoscalar field at the moments of photon emission and observation. For fields that vary slowly, this means that birefringence is proportional to the propagation length of photons [2, 8]. In that case, we can assume that the birefringence suffered by locally emitted Galactic foregrounds ($z \approx 0$) is negligible compared to that seen by CMB photons emitted at recombination ($z \approx 1100$). Thus, Galactic foreground emission would only be significantly affected by the α_i miscalibration, allowing us to break the degeneracy between both angles [42]. In this way, the E - and B - mode spherical harmonic coefficients of the observed signal at a certain frequency band ν_i would be

$$\begin{pmatrix} E_{\ell m}^{i,o} \\ B_{\ell m}^{i,o} \end{pmatrix} = \begin{pmatrix} c(2\alpha_i) & -s(2\alpha_i) \\ s(2\alpha_i) & c(2\alpha_i) \end{pmatrix} \begin{pmatrix} E_{\ell m}^{i,fg} \\ B_{\ell m}^{i,fg} \end{pmatrix} + \begin{pmatrix} c(2\alpha_i + 2\beta) & -s(2\alpha_i + 2\beta) \\ s(2\alpha_i + 2\beta) & c(2\alpha_i + 2\beta) \end{pmatrix} \begin{pmatrix} E_{\ell m}^{i,CMB} \\ B_{\ell m}^{i,CMB} \end{pmatrix}, \quad (2.1)$$

where the different superscripts stand for the observed signal (“o”), and the underlying Galactic foreground (“fg”) and CMB emissions. Note that in this equation, and throughout the rest of the paper unless otherwise stated, foreground and CMB spherical harmonic coefficients and angular power spectra are assumed to be convolved by the instrumental beam and pixel window functions corresponding to each frequency band.

Calculating the angular power spectra of the spherical harmonic coefficients in Eq. (2.1) leads to the following EE , BB , and EB cross-correlations between different i and j frequency bands:

$$\begin{pmatrix} C_{\ell}^{E_i E_j, o} \\ C_{\ell}^{E_i B_j, o} \\ C_{\ell}^{B_i E_j, o} \\ C_{\ell}^{B_i B_j, o} \end{pmatrix} = \mathbf{R}(\alpha_i, \alpha_j) \begin{pmatrix} C_{\ell}^{E_i E_j, fg} \\ C_{\ell}^{E_i B_j, fg} \\ C_{\ell}^{B_i E_j, fg} \\ C_{\ell}^{B_i B_j, fg} \end{pmatrix} + \mathbf{R}(\alpha_i + \beta, \alpha_j + \beta) \begin{pmatrix} C_{\ell}^{E_i E_j, \Lambda\text{CDM}} \\ 0 \\ 0 \\ C_{\ell}^{B_i B_j, \Lambda\text{CDM}} \end{pmatrix}, \quad (2.2)$$

where \mathbf{R} is the rotation matrix

$$\mathbf{R}(\theta, \theta') = \begin{pmatrix} c(2\theta)c(2\theta') & -c(2\theta)s(2\theta') & -s(2\theta)c(2\theta') & s(2\theta)s(2\theta') \\ c(2\theta)s(2\theta') & c(2\theta)c(2\theta') & -s(2\theta)s(2\theta') & -s(2\theta)c(2\theta') \\ s(2\theta)c(2\theta') & -s(2\theta)s(2\theta') & c(2\theta)c(2\theta') & -c(2\theta)s(2\theta') \\ s(2\theta)s(2\theta') & s(2\theta)c(2\theta') & c(2\theta)s(2\theta') & c(2\theta)c(2\theta') \end{pmatrix}. \quad (2.3)$$

In this work, we neglect CMB EB correlations prior to α_i or β rotations, since they are expected to be null in Λ CDM [14]. Nevertheless, in the case of working with alternative models that grant the CMB an initial EB correlation at the moment of recombination (e.g., chiral gravitational waves [14, 61, 62] or anisotropic inflation [63]), the corresponding EB terms must be added to the equations derived from Eq. (2.2), and a theoretical angular power spectrum must be provided for them. On the other hand, we do consider a potential intrinsic foreground EB correlation even though current experimental constraints find it to still be statistically compatible with zero [50, 51].

Starting from Eq. (2.2), we build a maximum likelihood estimator to simultaneously calculate β and α_i . Although we use the cross-spectra estimator throughout the rest of the work, in this section we adopt the simpler formulation in terms of only frequency auto-spectra ($i = j$ in Eq. (2.2)) to explain the methodology in detail. For the derivation of the more general estimator in terms of frequency cross-spectra see appendix A. Following a procedure similar to the one detailed in Refs. [13, 42, 60], the observed EB correlation is written as a rotation of the observed EE and BB angular power spectra, the Λ CDM prediction for the CMB EE and BB angular power spectra, and the foreground EB signal:

$$C_\ell^{EB,i,o} = \frac{t(4\alpha_i)}{2} \left(C_\ell^{EE,i,o} - C_\ell^{BB,i,o} \right) + \frac{\mathcal{A}}{c(4\alpha_i)} C_\ell^{EB,i,fg} + \frac{s(4\beta)}{2c(4\alpha_i)} \left(C_\ell^{EE,i,\Lambda\text{CDM}} - C_\ell^{BB,i,\Lambda\text{CDM}} \right). \quad (2.4)$$

Here \mathcal{A} is introduced *ad hoc* as a normalization parameter: we can set $\mathcal{A} = 0$ to ignore the foreground EB contribution, or take $\mathcal{A} = 1$ if the true foreground emission is known.

If the foreground contribution is considered ($\mathcal{A} \neq 0$), then Eq. (2.4) asks for the intrinsic foreground EB correlation prior to any potential α_i rotation. In this work, we take the **Commander** [55–58] sky model² derived from the analysis of an early version of *Planck* PR4 data as a template for the polarized foreground emission, leaving \mathcal{A} as a free amplitude parameter to fit alongside β and α_i . Here we consider a single overall amplitude and use **Commander** spectral energy distributions (SEDs) to scale the foreground template to the target frequencies. The methodology extends easily to different \mathcal{A}_i amplitudes for each frequency band, at the price of increasing the number of parameters to fit.

This approach warrants a couple of caveats. First, **Commander** does not yet provide a signal-dominated template for the foreground EB correlation [64, 65]. Hence the template might include some of the noise fluctuations present in *Planck* data. Second, the existence of miscalibrated polarization angles, which were not considered in the SEDs assumed by **Commander** to model Galactic foreground emission, might lead to a spurious EB correlation in their final foreground maps. However, we believe this effect to be minimal, since the EB measured in **Commander**'s dust template does not resemble a $s(4\alpha)(C_\ell^{EE,fg} - C_\ell^{BB,fg})/2$ rotation. To avoid such a spurious EB signal, parametric component-separation methodologies that include instrumental polarization angles in their SEDs are already being proposed [60]. Finally, the integration along the line-of-sight of the thermal emission from several dust clouds with different spectral parameters and polarization angles is not fully characterized by the single modified blackbody SED used by **Commander** [66–70]. This can create spurious dust EB correlations with a different frequency dependence and a strong dependence on the sky

²The foreground sky model used in this work can be found at NERSC under [/global/cfs/cdirs/cmb/data/planck2020/all_data/npipe6v20_sim/skymodel_cache](https://global.cfs.cdhrs.cmb/data/planck2020/all_data/npipe6v20_sim/skymodel_cache).

fraction and multipole range considered [71]. Alternative ways to model the foreground EB correlation without relying on templates have been proposed in Refs. [13, 42, 43, 49, 59].

From the equality in Eq. (2.4), we build a Gaussian likelihood to simultaneously fit for β , α_i , and \mathcal{A} . For a CMB experiment with a total of N_ν frequency bands, and using the $\chi_{ij\ell}^s = C_\ell^{E_i E_j, s} - C_\ell^{B_i B_j, s}$ abbreviation, that log-likelihood takes the form

$$-2 \ln \mathcal{L} \supset \sum_{i,j} \sum_{\ell, \ell'} \left[C_\ell^{EB, i, o} - \frac{t(4\alpha_i)}{2} \chi_{i\ell}^o - \frac{\mathcal{A}}{c(4\alpha_i)} C_\ell^{EB, i, fg} - \frac{s(4\beta)}{2c(4\alpha_i)} \chi_{i\ell}^{\Lambda\text{CDM}} \right] \times \\ \mathbf{C}_{ij\ell\ell'}^{-1} \left[C_{\ell'}^{EB, j, o} - \frac{t(4\alpha_j)}{2} \chi_{j\ell'}^o - \frac{\mathcal{A}}{c(4\alpha_j)} C_{\ell'}^{EB, j, fg} - \frac{s(4\beta)}{2c(4\alpha_j)} \chi_{j\ell'}^{\Lambda\text{CDM}} \right], \quad (2.5)$$

where we are summing over all possible combinations of detector channels ($i, j = 1, \dots, N_\nu$) and multipoles ($\ell, \ell' \in [\ell_{\min}, \ell_{\max}]$ for a total of $N_\ell = \ell_{\max} - \ell_{\min} + 1$), and $\mathbf{C}_{ij\ell\ell'}$ is the covariance matrix of $N_\nu N_\ell \times N_\nu N_\ell$ dimensions. Here we use the \supset symbol to remind the reader that Eq. (2.5) does not show the full log-likelihood, since the $\ln |\mathbf{C}_{ij\ell\ell'}|$ term is not included; although it can usually be excluded from the minimization process, in our case, the log-determinant must be taken into account because the model parameters explicitly appear in the covariance matrix. Therefore, the variation of the free parameters during minimization leads to a change in the likelihood's normalization that can bias the results if it is not correctly accounted for. As will be further discussed later in this section and in appendix B, the iterative algorithm we propose automatically accounts for this change, so that we do not need to explicitly consider the contribution of the log-determinant.

For each combination of ij frequency bands, the corresponding $N_\ell \times N_\ell$ box of the covariance is calculated as

$$\mathbf{C}_{ij\ell\ell'} = \text{Cov} \left[C_\ell^{EB, i, o} - \frac{t(4\alpha_i)}{2} \chi_{i\ell}^o - \frac{\mathcal{A}}{c(4\alpha_i)} C_\ell^{EB, i, fg} - \frac{s(4\beta)}{2c(4\alpha_i)} \chi_{i\ell}^{\Lambda\text{CDM}}, \right. \\ \left. C_{\ell'}^{EB, j, o} - \frac{t(4\alpha_j)}{2} \chi_{j\ell'}^o - \frac{\mathcal{A}}{c(4\alpha_j)} C_{\ell'}^{EB, j, fg} - \frac{s(4\beta)}{2c(4\alpha_j)} \chi_{j\ell'}^{\Lambda\text{CDM}} \right]. \quad (2.6)$$

Note that in Eq. (2.6), covariance elements are calculated from the observed angular power spectra and from the model for both foreground and CMB signals. Neglecting ℓ -to- ℓ' correlations and assuming that the spherical harmonic coefficients are Gaussian, we can approximate each box of the covariance between whatever X, Y, Z, and W combination of observed, foreground, or CMB E- and B-modes by its diagonal:

$$\text{Cov} [C_\ell^{XY}, C_{\ell'}^{ZW}] \approx \frac{1}{2\ell + 1} \delta_{\ell\ell'} (C_\ell^{XZ} C_\ell^{YW} + C_\ell^{XW} C_\ell^{YZ}). \quad (2.7)$$

In our notation, we explicitly indicate the use of this approximation by reducing $\mathbf{C}_{ij\ell\ell'}$ to $\mathbf{C}_{ij\ell}$, and summations in both ℓ and ℓ' to just ℓ . The impact that the non-Gaussianity of Galactic foregrounds has on the estimator was already studied in Ref. [60]. In the case of partial skies, one can still approximate the covariance matrix as diagonal as long as the ℓ -to- ℓ' correlations induced by the limited sky coverage are reduced by sufficiently apodizing the analysis mask and binning the angular power spectra. See appendix C for more details in the calculation of the covariance matrix. Finally, we average both the angular power spectra and the covariance

matrix into N_{bins} uniform bins of $\Delta\ell$ width:

$$C_b^X = \frac{1}{\Delta\ell} \sum_{\ell \in b} C_\ell^X, \quad \mathbf{C}_{ijb} = \frac{1}{\Delta\ell^2} \sum_{\ell \in b} \mathbf{C}_{ij\ell}. \quad (2.8)$$

In addition to reducing the coupling between non-diagonal multipoles for masked skies, binning also helps to reduce the numerical instabilities that arise from calculating the covariance matrix from observed spectra rather than from theoretical models [60]. In this work, we focus on high- ℓ data and uniformly bin angular power spectra and covariance matrices from $\ell_{\text{min}} = 51$ to $\ell_{\text{max}} = 1490$, with a spacing of $\Delta\ell = 20$ ($N_{\text{bins}} = 72$), to match the analysis in Ref. [49].

The likelihood in Eq. (2.5) is often sampled with Markov chain Monte Carlo (MCMC) methods to find the best-fit solution for all parameters, as done in Refs. [13, 42–44, 46, 49, 59]. As an extension of the methodology presented in Ref. [60], we propose an alternative iterative implementation to calculate the maximum likelihood solution for \mathcal{A} , β , and α_i semi-analytically. In this algorithm, we assume that the \mathcal{A} , β , and α_i parameters in the covariance matrix are known and fixed, starting at $\mathbf{x}_i = (\mathcal{A}, \beta, \alpha_i) = (1, 0, 0)$. Then, applying the small-angle approximation (valid for angles $\lesssim 10^\circ$), the likelihood in Eq. (2.5) is reduced to

$$-2 \ln \mathcal{L} \supset \sum_{i,j} \sum_b \left[C_b^{EB,i,o} - 2\alpha_i \chi_{iib}^o - \mathcal{A} C_b^{EB,i,fg} - 2\beta \chi_{iib}^{\Lambda\text{CDM}} \right] \times \\ \mathbf{C}_{ijb}^{-1} \left[C_b^{EB,j,o} - 2\alpha_j \chi_{jjb}^o - \mathcal{A} C_b^{EB,j,fg} - 2\beta \chi_{jjb}^{\Lambda\text{CDM}} \right]. \quad (2.9)$$

Differentiating Eq. (2.9) with respect to each of the \mathbf{x}_i parameters, we obtain a set of linear equations with which to calculate the maximum likelihood solution for all parameters analytically. This first estimate is then used to update the covariance matrix and recalculate a new best-fit solution, starting an iterative process that converges after only a few iterations. By fixing the value of the free parameters in the covariance matrix and iteratively updating them, we are implicitly accounting for the change in the likelihood's normalization that would otherwise need to be explicitly considered through the inclusion of the $\ln |C_{ij\ell}|$ term in Eqs. (2.5) and (2.9). With this algorithm, we achieve a great reduction of execution time without losing accuracy and precision with respect to the MCMC sampling of the full likelihood. See appendix B for a more detailed comparison of both implementations.

In particular, the minimization of Eq. (2.9) leads to a linear system $\sum_n \mathbf{A}_{mn} \mathbf{x}_n = \mathbf{b}_m$ of the form:

$$\left(\begin{array}{c|c|c} \Xi & Z & K_n \dots \\ \hline Z & \Theta & T_n \dots \\ \hline K_m & T_m & \Omega_{mn} \\ \vdots & \vdots & \end{array} \right) \begin{pmatrix} \mathcal{A} \\ \beta \\ \alpha_n \\ \vdots \end{pmatrix} = \begin{pmatrix} \xi \\ \theta \\ \omega_m \\ \vdots \end{pmatrix}, \quad (2.10)$$

where the elements of the \mathbf{A}_{mn} system matrix are

$$\Xi = \sum_{i,j} \sum_b C_b^{EB,i,fg} \mathbf{C}_{ijb}^{-1} C_b^{EB,j,fg}, \quad (2.11)$$

$$Z = 2 \sum_{i,j} \sum_b C_b^{EB,i,fg} \mathbf{C}_{ijb}^{-1} \chi_{jjb}^{\Lambda\text{CDM}}, \quad (2.12)$$

$$\Theta = 4 \sum_{i,j} \sum_b \chi_{iib}^{\Lambda\text{CDM}} \mathbf{C}_{ijb}^{-1} \chi_{jjb}^{\Lambda\text{CDM}}, \quad (2.13)$$

$$K_m = 2 \sum_j \sum_b \chi_{mmb}^o \mathbf{C}_{mjb}^{-1} C_b^{EB,j,fg}, \quad (2.14)$$

$$T_m = 4 \sum_j \sum_b \chi_{mmb}^o \mathbf{C}_{mjb}^{-1} \chi_{jjb}^{\Lambda\text{CDM}}, \quad (2.15)$$

$$\Omega_{mn} = 4 \sum_b \chi_{mmb}^o \mathbf{C}_{mmb}^{-1} \chi_{nnb}^o, \quad (2.16)$$

and \mathbf{b}_m terms that are

$$\xi = \sum_{i,j} \sum_b C_b^{EB,i,fg} \mathbf{C}_{ijb}^{-1} C_b^{EB,j,o}, \quad (2.17)$$

$$\theta = 2 \sum_{i,j} \sum_b C_b^{EB,i,o} \mathbf{C}_{ijb}^{-1} \chi_{jjb}^{\Lambda\text{CDM}}, \quad (2.18)$$

$$\omega_m = 2 \sum_j \sum_b \chi_{mmb}^o \mathbf{C}_{mjb}^{-1} C_b^{EB,j,o}. \quad (2.19)$$

Finally, this formalism allows us to calculate the uncertainty associated with the maximum likelihood solution within the Fisher matrix approximation. The corresponding covariance matrix is $\mathbf{C}_{mn}^{-1} = -\frac{\partial^2 \ln \mathcal{L}}{\partial x_m \partial x_n} = \mathbf{A}_{mn}$.

3 NPIPE simulations and Galactic masks

We use the official NPIPE end-to-end simulations³ of *Planck*'s HFI 100, 143, 217, and 353GHz bands to test the robustness of our methodology against Galactic foreground emission and instrumental systematics in a realistic scenario. The NPIPE release [48] provides a set of high-fidelity Monte Carlo simulated maps that include CMB, Galactic foregrounds, noise, and systematics. Simulations of detector splits, obtained by dividing the horns in the focal plane into two subsets (A and B) and independently processing them, are also provided.

The CMB realizations are the full-focal plane simulations used in PR3 [72]. Galactic foregrounds are simulated by evaluating the **Commander** sky model derived from the analysis of an early version of NPIPE data at the target frequencies. In particular, synchrotron radiation is modeled with a power-law SED, and thermal dust emission as a one-component modified blackbody. When the angular resolution of the foreground model is higher than that of the target frequency band (e.g., dust at 100GHz), the foreground component is smoothed to match the **QuickPol** [73] beam specific to the NPIPE dataset. To avoid divergences in the deconvolution, the Gaussian beam with full-width-at-half-maximum (FWHM) of 5 arcmin present in **Commander**'s dust component is maintained at 217 and 353GHz. Static zodiacal emission is also included by adding the same nuisance templates that **Commander** marginalized over. Among other instrumental effects, noise maps include beam systematics, gain calibration and bandpass mismatches, analogue-to-digital conversion non-linearities, and the transfer-function corrections. Noise maps also capture the non-linear response of the instrument and of the NPIPE processing pipeline, reproducing the non-linear couplings between signal and noise that they introduce. Please refer to Ref. [48] for a more detailed description of the systematic effects included in NPIPE simulations.

³The foreground sky model and the simulations used in this paper (individual input components as well as coadded maps) are available at NERSC under /global/cfs/cdirs/cmb/data/planck2020/all_data.

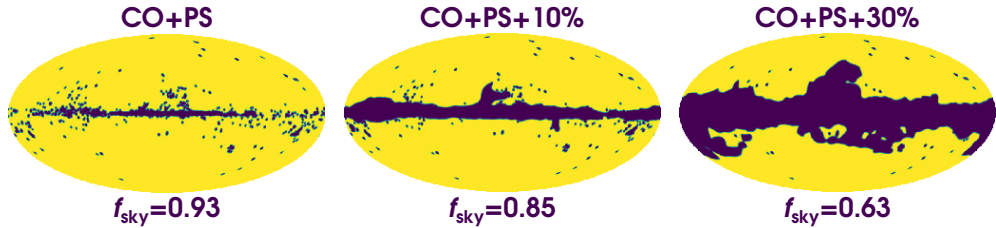


Figure 1: Galactic masks considered in this work. They are three of the five masks used in Ref. [49] for the analysis of *Planck* HFI data.

For the analysis presented in section 4, we build a first simulation set ($\text{FG}^\alpha + \text{CMB}^{\alpha+\beta} + \text{N}$) by coadding foreground maps with 100 different CMB realizations and their associated noise maps. Before addition, foreground and CMB maps are rotated by α_i and $\alpha_i + \beta$ angles, respectively. For each realization, birefringence and polarization angles are randomly drawn from a uniform distribution in the range $[-1^\circ, 1^\circ]$. To mimic the analysis in Ref. [49], we simulate A/B detector splits with a different miscalibration angle per split, i.e., α_i with $i = 100\text{A}, 100\text{B}, \dots, 353\text{B}$. In other words, we treat A/B detector splits as if they were observations from different frequency bands.

To assess the impact of instrumental systematics different from a miscalibration of polarization angles, we build a second simulation set ($\text{CMB} + \text{N}$) by coadding the same 100 CMB realizations and their associated noise maps. In this case we do not rotate the maps, since we want to use them to test whether some of the systematic effects in the NPIPE data lead to any systematic β or α_i angles. This second simulation set is also generated for A/B detector splits.

We adopt three of the masks used in the analysis of *Planck* HFI data presented in Ref. [49] (see figure 1). The default mask is built by masking point sources and the regions where the emission of the carbon monoxide (CO) line is the brightest. The common point-source mask is constructed from the combination of the *Planck* point source-polarization masks⁴ at 100, 143, 217, and 353GHz. Pixels where the CO line is brighter than $45 \text{ K}_{\text{RJ}}\text{kms}^{-1}$ are also masked because, although CO is not polarized, the mismatch of detector bandpasses creates a spurious polarization signal via intensity-to-polarization leakage. While CO strength varies over frequency, a common CO mask is adopted for all channels to simplify the analysis. This base CO+PS mask is then extended to exclude 10% and 30% of the regions of brightest Galactic foreground emission by thresholding the NPIPE 353GHz polarization and total intensity maps smoothed with a Gaussian beam with a FWHM of 10° . Finally, all masks are apodized with a 1° FWHM Gaussian. The effective sky fraction to use in the calculation of the covariance matrix is given by $f_{\text{sky}} = N_{\text{pix}}^{-1} (\sum_i \omega_i^2)^2 / (\sum_i \omega_i^4)$ [74, 75], where ω_i is the value of the (non-integer) apodized mask, and N_{pix} is the total number of pixels. This yields $f_{\text{sky}} = 0.93, 0.85,$ and 0.63 for the CO+PS, CO+PS+10%, and CO+PS+30% masks, respectively.

In our analysis of masked skies, we calculate full-sky pseudo- C_ℓ s using NaMaster⁵ [76] and without performing any E/B mode purification⁶. For the CO+PS+30% mask, we bin the pseudo- C_ℓ calculated with NaMaster to reduce the ℓ -to- ℓ' correlations induced by the partial sky coverage, so than we can still approximate the covariance matrix as diagonal.

⁴HFI_Mask_PointSrc_2048_R2.00.fits file at <https://pla.esac.esa.int/#maps>.

⁵<https://github.com/LSSTDESC/NaMaster>

⁶We do not perform E/B mode purification because the E -to- B leakage produced by our masks of $f_{\text{sky}} \gtrsim 60\%$ is negligible at the angular scales $\ell > 50$ used in our analysis.

4 Impact of Galactic foregrounds

To determine the impact of Galactic foregrounds on the measurement of cosmic birefringence, we apply our frequency cross-spectra-only estimator (see appendix A) to the $100 \text{ FG}^\alpha + \text{CMB}^{\alpha+\beta} + \text{N}$ simulations and calculate the difference between the true input angles and the estimated ones. Figures 2 and 3 show the typical bias in angle estimation, where data points correspond to the mean value and uncertainties are calculated as the simulations' dispersion (one standard deviation).

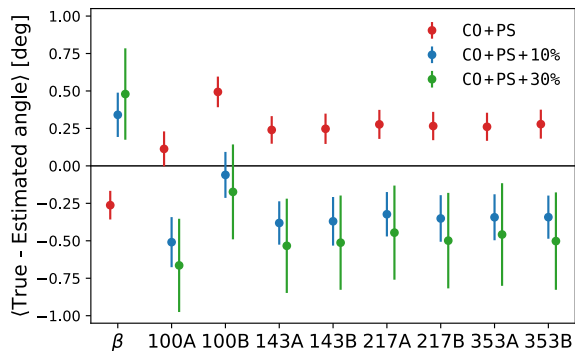


Figure 2: Bias in the simultaneous estimation of birefringence and miscalibration angles from $\text{FG}^\alpha + \text{CMB}^{\alpha+\beta} + \text{N}$ simulations when the foreground EB correlation is neglected. Uncertainties are calculated as the simulations' dispersion (one standard deviation). Results are shown for the three Galactic masks considered in this work.

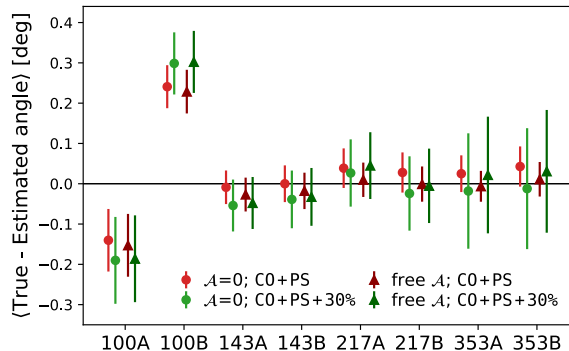


Figure 3: Bias in the estimation of exclusively miscalibration angles from $\text{FG}^\alpha + \text{CMB}^{\alpha+\beta} + \text{N}$ simulations with $\beta = 0$. We show results for the case where the foreground EB correlation is neglected (circles) and considered (triangles), and only for our smallest (red) and largest (green) masks. Uncertainties are calculated as the simulations' dispersion.

As in previous works [42–44, 46], we start by neglecting the foreground EB contribution in figure 2. Those results demonstrate that β and α_i measurements are biased when both angles are estimated simultaneously and the foreground EB is not acknowledged. In contrast, figure 3 shows the typical bias that we obtain from $\text{FG}^\alpha + \text{CMB}^{\alpha+\beta} + \text{N}$ simulations with $\beta = 0$ when estimating miscalibration angles alone, for the case in which the foreground EB is ignored ($\mathcal{A} = 0$) or modeled by providing a template for foreground emission (free \mathcal{A}). The good agreement between the results obtained in both cases demonstrates that assuming a null foreground EB correlation does not introduce any significant bias to the measurement of exclusively miscalibration angles. This was also shown by Ref. [60] in the context of the LiteBIRD satellite. The only exceptions are the systematic α_i angles found for the 100A and 100B detector splits. As discussed in the next section, those systematic angles do not reflect a bias of our methodology but rather reveal the presence of a cross-polarization effect in NPIPE simulations.

To clarify the reason behind their different response to foreground EB , figure 4 shows the signal-to-noise ratio per bin obtained for the different rotation angles with estimators that measure exclusively miscalibration angles (left), or both birefringence and miscalibration angles simultaneously (right). The signal-to-noise ratio associated with each x_m variable is calculated as $S/N_b(x_m) = x_m / (\sum_{b' \in w_b} C_{mm'b'})^{1/2}$, where w_b is a square window function of

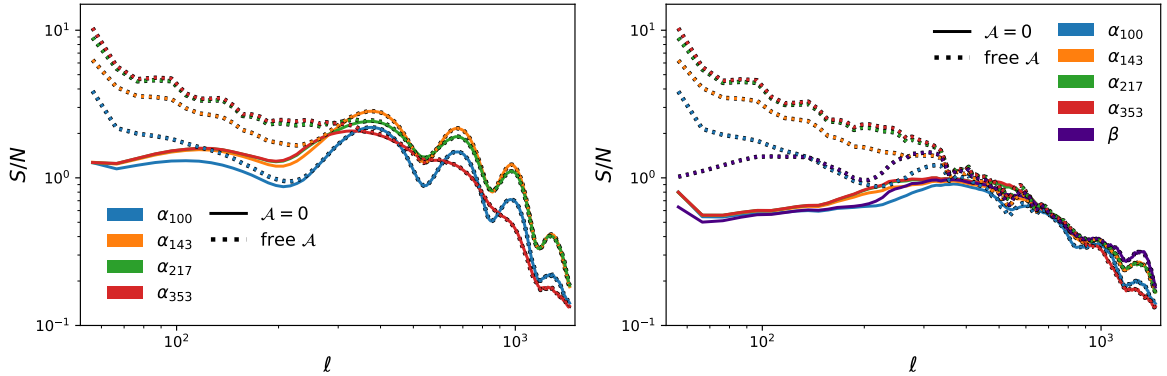


Figure 4: Signal-to-noise ratio per bin when determining exclusively miscalibration angles (left), or both birefringence and miscalibration angles simultaneously (right). Results are shown for the case where the foreground EB is ignored (solid lines), or a foreground template is provided (dashed lines). The S/N shown for miscalibration angles is the average of both A/B detector splits. S/N ratios were calculated for one $FG^\alpha + CMB^{\alpha+\beta} + N$ simulation with $\beta = \alpha_i = 0.3^\circ$ and using the CO+PS mask.

$\Delta b = 10$ centered around each bin, and the covariance is the $C_{mn} = A_{mn}^{-1}$ matrix defined in appendix A. The bin-dependence (and, by extension, ℓ -dependence) in C_{mnb} comes from removing the summation in b from Eqs. (A.8) to (A.16). The main difference between both estimators is that, when focused exclusively on the determination of miscalibration angles (left panel of figure 4), information can be gathered from all scales, since both Galactic foregrounds and the CMB are rotated by α . In this sense, providing a template of foreground emission increases the S/N at $\ell \lesssim 300$ scales, but dismissing the contribution of the foreground EB correlation does not lead to a significant bias.

On the other hand, when trying to simultaneously determine both birefringence and miscalibration angles, we rely on foregrounds to determine α_i and partially break the degeneracy between both effects. Thus, a precise knowledge of foreground emission is crucial, especially at the $\ell \lesssim 300$ foreground-dominated scales. In the right panel of figure 4, we see that when no foreground template is provided, the S/N ratio of β (purple solid line) shows the same angular dependence at large-scales as that of miscalibration angles (rest of colored solid lines), indicating that β is being derived from foregrounds as well as the CMB. As a consequence, the unaccounted foreground EB produces the bias seen in the left panel of figure 5 (blue contours), where we show the correlation between the β and α_{353B} ⁷ angles recovered when only $\ell < 300$ scales are used. After a template for the foreground EB is provided, we see that such a bias is reduced (orange contours), and that now the angular dependence of the S/N ratios of β and α_i angles (dotted colored lines) correctly resemble those of, respectively, the CMB and Galactic foreground signals in the right panel of figure 4. In addition, the extra knowledge on foreground emission provided by the template helps to break the degeneracy between β and α_i angles, relaxing the anti-correlation between them from $\rho \approx -0.9$ to $\rho \approx -0.40$.

At small angular scales ($\ell \gtrsim 300$), the CMB starts to dominate over the foreground emission and becomes the common source of S/N for both β and α_i . At those scales, there is

⁷Here we chose α_{353B} as an example of a foreground-dominated band, but similar correlations are found across the rest of the detector splits.

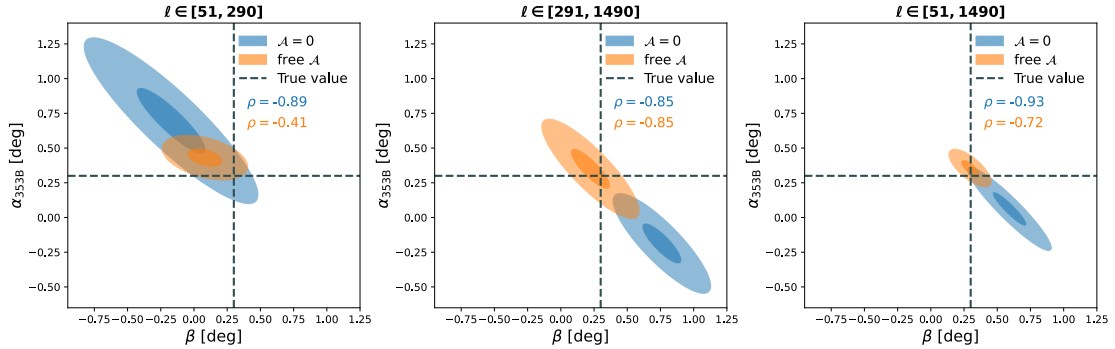


Figure 5: Correlation between β and α_{353B} angles simultaneously determined from a $\text{FG}^\alpha + \text{CMB}^{\alpha+\beta} + \text{N}$ simulation with $\beta = \alpha_i = 0.3^\circ$ (dashed lines) analyzed with the CO+PS mask. Results on the left correspond to the study of only large-scale information, those in the center to only small-scale information, and those on the right combine the information from all scales. Blue ellipses show the 1σ and 2σ Fisher confidence contours obtained when the foreground EB is ignored, while the orange ones are those obtained when a foreground template is provided. Correlation coefficients are given for both cases.

not enough foreground signal to break the degeneracy between both angles, but the inclusion of the template still helps to avoid the bias induced by the foreground EB correlation (central panel of figure 5). Once all scales are included in the analysis (right panel of figure 5), the extra constraining power that the template grants at large-scales helps to alleviate the degeneracy between both angles (from $\rho \approx -0.90$ to $\rho \approx -0.70$) and correct the bias induced by the foreground EB correlation, bringing the best-fit value closer to the correct answer. In this way, ignoring the foreground EB correlation when simultaneously estimating β and α_i angles leads to the biases seen in figure 2.

We also check the correct performance of the estimator by comparing the uncertainty obtained from the simulations' dispersion with that of the Fisher prediction. That is what we do in figure 6, where data points show the uncertainty calculated as the simulations' dispersion (σ_{sim}) and solid lines correspond to the Fisher matrix prediction (σ_{Fisher}). We expect the Fisher formalism to overestimate σ_{sim} uncertainties as seen for the CO+PS (red) and CO+PS+10%

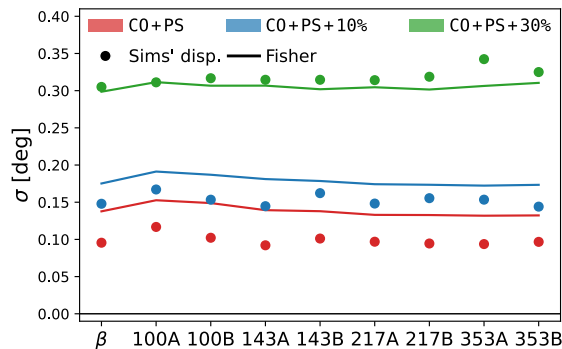


Figure 6: Comparison between simulations- (circles) and Fisher-derived (solid lines) uncertainties when birefringence and miscalibration angles are simultaneously estimated from $\text{FG}^\alpha + \text{CMB}^{\alpha+\beta} + \text{N}$ simulations and the foreground EB correlation is neglected.

(blue) masks, since foreground emission is a source of cosmic variance in our covariance matrix but we have used a common foreground realization for all of the $\text{FG}^\alpha + \text{CMB}^{\alpha+\beta} + \text{N}$ simulations. When the majority of Galactic emission is removed from the covariance with the CO+PS+30% mask (green), σ_{sim} and σ_{Fisher} uncertainties do agree.

Both the biases in the estimation of β and α_i angles and the inconsistencies between simulations- and Fisher-derived uncertainties are corrected when an accurate template for foreground emission is provided and \mathcal{A} is left as a free amplitude parameter in the likelihood. Figure 7 shows that now the mean values of the recovered β and α_i are centered around zero, with the exception of the aforementioned $\alpha_{100\text{A}}$ and $\alpha_{100\text{B}}$ systematic angles. Moreover, as is discussed in appendix D, providing a template for foreground emission allows for the removal of most of the variance originated by the foregrounds' fluctuations. The effects of removing the contribution of foreground emission from the covariance are twofold. First, it leads to a reduction of the total covariance that explains the smaller uncertainties seen in figure 8 with respect to those in figure 6. And second, it ensures that the uncertainties estimated from the simulations' dispersion and the Fisher analysis are compatible with each other for all of the three Galactic masks. This last observation does not just apply to our simulations with a fixed foregrounds realization. It is a feature transferable to the analysis of real data. If we believe that our template is a measurement of the true foreground signal in the sky, then its cosmic variance should not contribute to the total uncertainty. Within this interpretation, the emission of our Galaxy is explicitly characterized at the map level through the template, while the CMB signal is only statistically characterized by the theoretical angular power spectra provided.

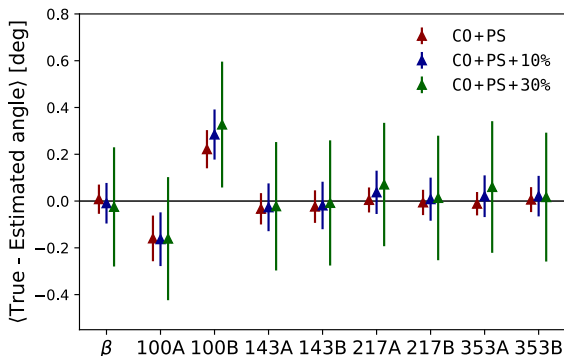


Figure 7: Bias in the simultaneous estimation of birefringence and miscalibration angles from $\text{FG}^\alpha + \text{CMB}^{\alpha+\beta} + \text{N}$ simulations when a template for foreground emission is provided. Uncertainties are calculated as the simulations' dispersion (one standard deviation).

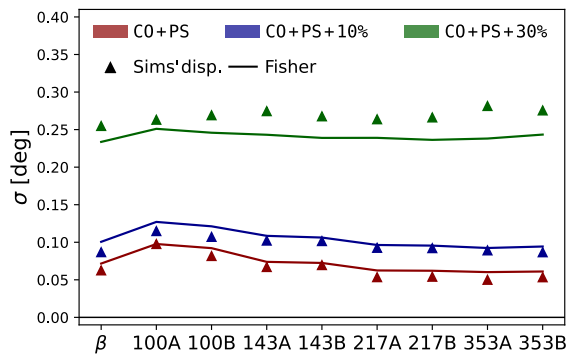


Figure 8: Comparison between simulations- (triangles) and Fisher-derived (solid lines) uncertainties when birefringence and miscalibration angles are simultaneously estimated from $\text{FG}^\alpha + \text{CMB}^{\alpha+\beta} + \text{N}$ simulations and a foreground template is provided.

The amplitude of the foreground template is also correctly recovered, with uncertainties from Fisher analysis and the simulations' dispersion nicely matching, as can be seen in figure 9. In our case, the recovered amplitudes are centered around unity because the foreground template is the same as the fiducial foreground model used in the simulations. We checked that the choice of initial value for \mathcal{A} does not condition the final results. Here we started from $\mathcal{A} = 1$, but the algorithm quickly converges to compatible results after a couple more iterations when starting from $\mathcal{A} \in \{-1, 0\}$. These results show that, with the exception of

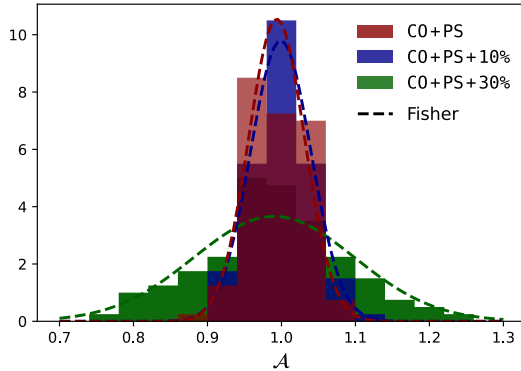


Figure 9: Distribution of template amplitudes recovered from $\text{FG}^\alpha + \text{CMB}^{\alpha+\beta} + \text{N}$ simulations. For comparison, dashed lines show the Gaussian distribution predicted by the Fisher analysis.

the systematic $\alpha_{100\text{A}}$ and $\alpha_{100\text{B}}$ angles, our methodology provides an unbiased estimation of both birefringence and polarization angles, once the foreground EB is taken into account.

Finally, we can use the insight gained from this study of realistic simulations to interpret the results obtained from the analysis of *Planck* HFI data made in Ref. [49]. For that purpose, figure 10 reproduces some of the results of that publication, including the birefringence measurement obtained from *Planck* data without accounting for the EB correlation of Galactic dust (orange circles), and those obtained when correcting for dust EB using either the **Commander** sky model (purple triangles) or the filament model presented in Refs. [13, 49] (black triangles). Uncertainties are calculated within the Fisher approximation. The results for the CO+PS+30% mask ($f_{\text{sky}} = 0.63$) differ⁸ from those reported in Ref. [49], since now we have binned the pseudo- C_ℓ s calculated for this mask to further reduce ℓ -to- ℓ' correlations and have a more diagonal covariance matrix.

When dust EB is ignored, the decreasing values of β found as we enlarge the Galactic mask seem to qualitatively agree with the biases expected from figure 2. Having statistically characterized the bias produced by dust EB , we can de-bias those measurements by adding to them the mean bias calculated from the $\text{FG}^\alpha + \text{CMB}^{\alpha+\beta} + \text{N}$ simulations. This leads to the shaded orange squares, which are centered at the de-biased measurements and contain all values compatible with them at 1σ . De-biased values are compatible with the results obtained with both the filament and **Commander** models for $f_{\text{sky}} < 0.90$. The disagreement seen at higher f_{sky} suggests that the **Commander** template might be struggling to reproduce dust emission near the center of the Galactic plane where the single modified blackbody model may be too simplistic [68, 70, 71, 77, 78].

We also find that the reduction of uncertainties that we achieve by including the foreground template in the analysis of *Planck* data is larger than expected from the simulation study. To illustrate this discrepancy, the gray error bars around the birefringence measurements obtained with the **Commander** template in figure 10 show the uncertainty expected from the reduction seen in the simulation study, while the purple error bars show the actual uncertainty obtained in the fit to *Planck* data. In particular, uncertainties are underestimated by approximately a 18%, 23%, and 28% at $f_{\text{sky}} = 0.93$, 0.85, and 0.63, respectively. The

⁸The differences in the β angle measured with and without binning are of the order of $\Delta\beta \approx 0.3\sigma$ when dust EB is ignored or corrected with the filament model, and of $\Delta\beta \approx 0.6\sigma$ when corrected with the **Commander** sky model.

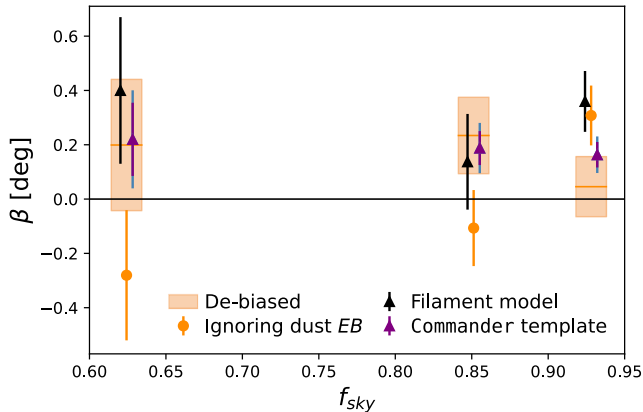


Figure 10: Birefringence measurements obtained from *Planck* HFI data without accounting for the EB correlation of Galactic dust, before (orange circles) and after (shaded orange squares), a posteriori correcting them with the dust EB bias estimated from $FG^\alpha + CMB^{\alpha+\beta} + N$ simulations. We also show the measurements obtained when dust EB is modeled using either the filament model presented in Refs. [13, 49] (black triangles) or **Commander**'s dust template (purple triangles). Gray error bars around measurements obtained with the **Commander** template show the uncertainty expected from the simulation study, while purple error bars show the actual uncertainty from the fit to *Planck* data.

fact that uncertainties are smaller in the analysis of the data than in the analysis of simulations where **Commander** is the fiducial foreground model suggests that the template might reproduce not only foreground emission but also some of the statistical fluctuations and noise from *Planck* data. In this way, the limited signal-to-noise of the **Commander** template leads to the over-reduction of the covariance matrix and the subsequent underestimation of error bars. Future experiments such as LiteBIRD [39] will provide high-precision measurements of the CMB polarization that will allow us to derive a signal-dominated dust template on the full-sky.

5 Impact of instrumental systematics

The miscalibration of polarization angles is not the only instrumental effect that interferes with the measurement of cosmic birefringence. Systematic effects like intensity-to-polarization leakage, beam leakage, or cross-polarization effects also produce spurious EB correlations that can bias our analysis. Since the effect of miscalibration angles and Galactic foregrounds was already determined in the previous section, here we use $CMB + N$ simulations to focus on the impact of the rest of systematics.

By construction, $CMB + N$ simulations reproduce the non-linear response of the instrument and the NPIPE processing pipeline, including the systematics produced by the non-linear couplings between signal and noise [48]. Therefore, $CMB + N$ simulations retain the systematics associated with foregrounds (e.g., the intensity-to-polarization leakage induced by the CO bandpass mismatch), despite discarding foreground emission itself. However, without foregrounds, we are no longer able to break the degeneracy between birefringence and miscalibration angles. Hence, instead of fitting them simultaneously, we must fit for β and α_i independently: we can fit a different angle for each detector split (see Ref. [60]), knowing that these effective α_i yield $\alpha_i + \beta$; or we can fit the same angle for all frequency bands

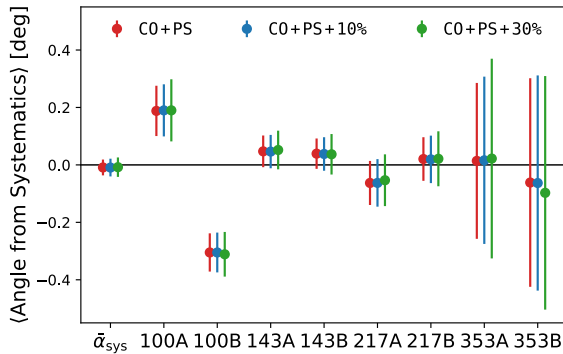


Figure 11: Mean α_i^{sys} and $\bar{\alpha}_{\text{sys}}$ angles found in CMB + N simulations with the cross-spectra-only estimator. Uncertainties are calculated as the simulations’ dispersion.

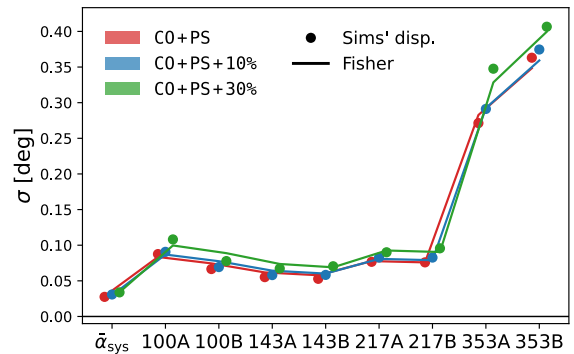


Figure 12: Comparison between the uncertainties derived from the dispersion of CMB + N simulations (points) and the Fisher analysis (solid lines).

(see Eq. (1.3)), obtaining an effective birefringence angle $\beta + \bar{\alpha}$ that includes the weighted average of miscalibration angles across all detector splits. Since CMB + N simulations do not contain birefringence or miscalibration angles, we know that any effective α_i found in them are produced by the rest of the systematic effects included in the simulations, with $\bar{\alpha}$ being the net effect of those systematics in the measurement of birefringence. We refer to these angles as α_i^{sys} and $\bar{\alpha}_{\text{sys}}$.

Fitting α_i^{sys} and $\bar{\alpha}_{\text{sys}}$ angles to the 100 CMB + N simulations with our frequency cross-spectra-only estimator, we obtain the mean angles shown in figure 11. Their corresponding uncertainties, calculated both as the simulations’ dispersion and within the Fisher approximation, are shown in figure 12. At a first glance, uncertainties now rapidly increase at 353GHz, a behaviour that differs from the one seen in figure 8. Such difference is explained by the absence of foregrounds in CMB + N simulations. Without foregrounds, rotation angles are estimated from the CMB, with instrumental noise as the only impediment. In this scenario, the larger uncertainties at 353GHz just reflect the configuration of *Planck*-HFI. 100, 143, and 217GHz frequency bands have similar noise levels around $1.5\mu\text{K}\cdot\text{deg}$, while the 353GHz band has $7.3\mu\text{K}\cdot\text{deg}$ [79]. Accordingly, the uncertainties recovered for 353B are approximately 6 times higher than those at, e.g., 143B, matching the roughly 6 times higher nominal noise level at 353GHz. In addition, masking the Galactic plane does not have such a dramatic effect as in figure 8, because here we are fitting effective $\alpha_i + \beta$ angles instead of using foregrounds to break the degeneracy between α_i and β . Still, uncertainties do scale as, roughly, $f_{\text{sky}}^{-1/2}$.

More quantitatively, we find that NPIPE systematics produce angles $\langle\alpha_{100A}^{\text{sys}}\rangle = 0.188^\circ \pm 0.009^\circ$ and $\langle\alpha_{100B}^{\text{sys}}\rangle = -0.305^\circ \pm 0.007^\circ$, with uncertainties given as the error of the mean. Although the values of α_i^{sys} are determined to high precision using CMB + N simulations, we would only be able to detect them at a 1.9-3.8 σ confidence level when simultaneously fitting β and α_i to real data (compare with the uncertainties on figure 8), and that is assuming that *Planck*’s polarimeters were perfectly calibrated. At other frequencies, $\langle\alpha_{143A}^{\text{sys}}\rangle = 0.047^\circ \pm 0.006^\circ$, $\langle\alpha_{143B}^{\text{sys}}\rangle = 0.039^\circ \pm 0.005^\circ$, and $\langle\alpha_{217A}^{\text{sys}}\rangle = -0.063^\circ \pm 0.008^\circ$ angles are also found at a lower significance level (0.6-1.3 σ compared to uncertainties on figure 8). These angles, produced by systematics, explain the biases seen in figures 2, 3, and 7. Note the change of sign, since those figures approximately show $-\langle\alpha_i^{\text{sys}}\rangle$.

To understand the origin of the α_i^{sys} angles seen in figure 11, we performed a closer

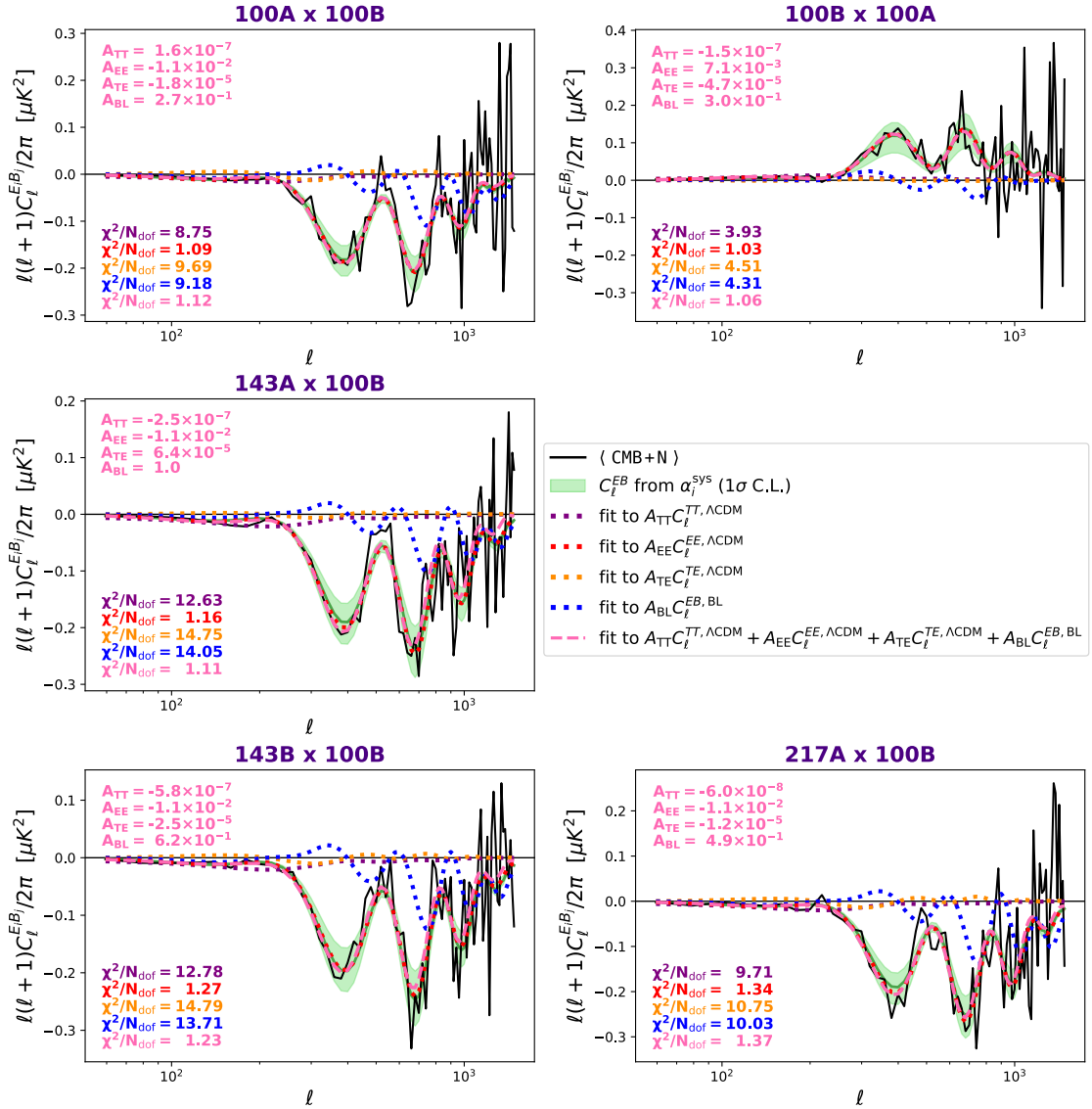


Figure 13: EB angular power spectra of CMB+N simulations (black solid lines) obtained from the cross-correlation of a selection of detector splits where cross-polarization is found to be the main systematic effect. Spectra were calculated using the CO+PS mask, averaged over 100 simulations, and binned in the range $\ell \in [51, 1490]$ with $\Delta\ell = 20$. Superimposed are the best fits to the different M_b models considered (dashed colored lines). The goodness of fit of each model is quantified by the reduced χ^2 shown in the bottom-left corner of every graph, and the values of the A_{TT} , A_{EE} , A_{TE} , and A_{BL} amplitudes obtained from the fit to Eq. (5.6) are specified in the top-left corner. Green shaded regions illustrate the 1σ confidence contours of the EB correlation expected from the α_i^{sys} angles found in figure 11.

study of the angular power spectra of CMB + N simulations. In particular, we investigate the origin of the $\alpha_{100\text{A}}^{\text{sys}}$ and $\alpha_{100\text{B}}^{\text{sys}}$ angles in figure 13, and that of the $\alpha_{143\text{A}}^{\text{sys}}$, $\alpha_{143\text{B}}^{\text{sys}}$, and $\alpha_{217\text{A}}^{\text{sys}}$ angles in figure 14. For completeness, in figure 15 we also show the angular power spectra of frequency bands where no significant α_i^{sys} is found. Black solid lines in figures 13, 14, and

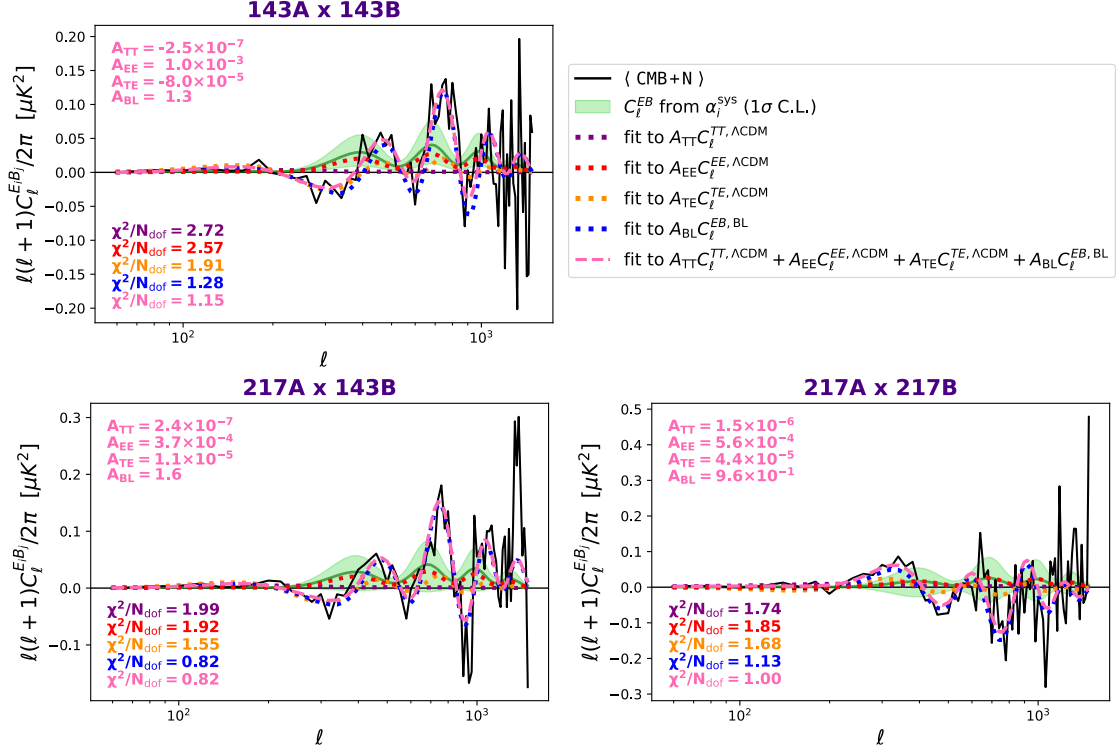


Figure 14: Same as figure 13 but for a selection of detector splits where beam leakage is found to be the main systematic effect.

15 show the mean C_ℓ^{EB} angular power spectra for a selection of bands, averaged over the 100 simulations, and binned in uniform bins from $\ell_{\min} = 51$ to $\ell_{\max} = 1490$ with a spacing of $\Delta\ell = 20$. We find no significant difference between mean CMB+N spectra calculated with the CO+PS, CO+PS+10%, or CO+PS+30% masks. Thus, we only display the spectra obtained with the CO+PS mask. As demonstrated in figures 13 and 14, even in the absence of an α_i miscalibration, CMB+N simulations present a spurious EB correlation between multipoles 200 and 1000 (corresponding roughly to angular scales between 50 and 10 arcmin). These features are more prominent at the lower frequencies, with cross-correlations involving 353GHz showing a mostly uncorrelated EB cross-spectra (see figure 15).

Those spurious EB correlations could be produced by several systematic effects. In general, intensity-to-polarization leakage gives $C_\ell^{EB} \propto C_\ell^{TT}$ at leading order, whereas the cross-polarization effect gives $C_\ell^{EB} \propto C_\ell^{EE}$. A combination of the two would give $C_\ell^{EB} \propto C_\ell^{TE}$. Beam imperfections and mismatches between each detector’s optical and electronic responses also lead to a leakage of signal into EB . For these simulations that contain only CMB and noise, we calculate the effect that beam leakage has on EB :

$$C_\ell^{EB, BL} = \omega_{\text{pix}, \ell}^2 \sum_{XY} W_\ell^{EB, XY} C_\ell^{XY, \Lambda\text{CDM}}, \quad (5.1)$$

where $XY \in \{TT, EE, BB, TE\}$, $\omega_{\text{pix}, \ell}$ is the pixel window function, and $W_\ell^{EB, XY}$ are the beam-window matrices calculated with QuickPol [73] specifically for *Planck* beams. To identify which of these effects is most likely to have caused the spurious EB correlations seen in

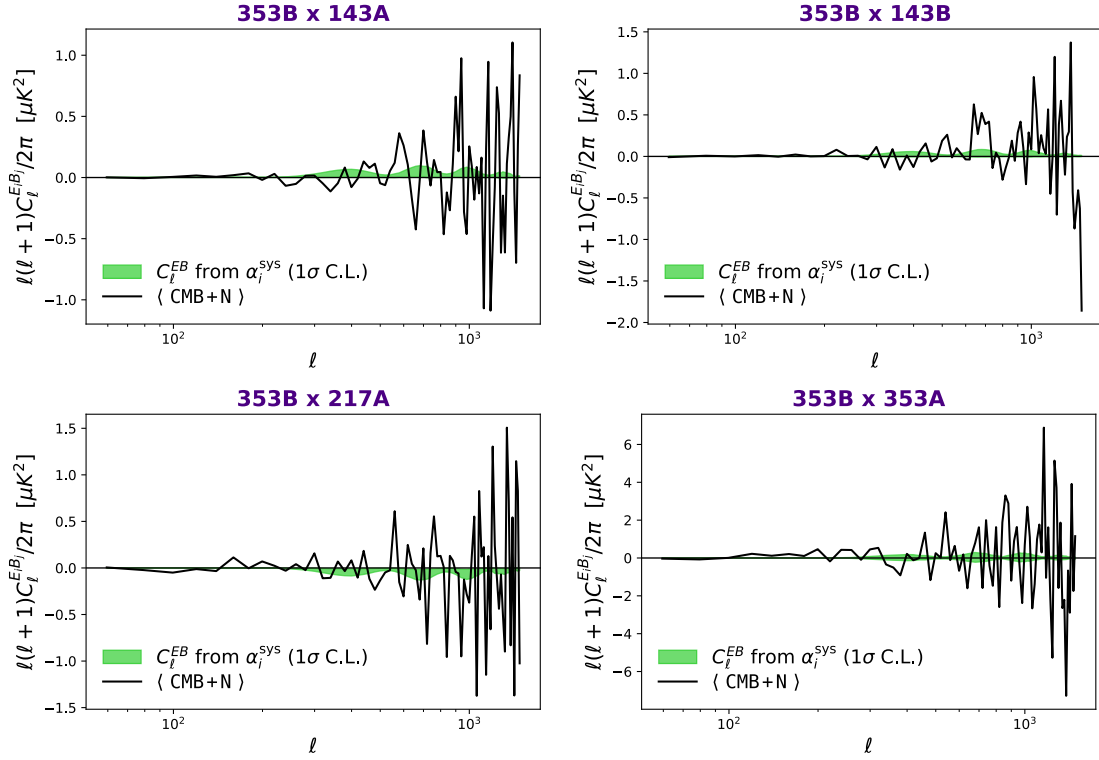


Figure 15: Same as figure 13 but for a selection of detector splits where systematics do not seem to produce a significant spurious EB correlation.

figures 13 and 14, we fit the mean CMB+N angular power spectra with the set of models

$$M_b \in \{A_{\text{TT}}C_b^{TT, \Lambda\text{CDM}}, \quad (5.2)$$

$$A_{\text{EE}}C_b^{EE, \Lambda\text{CDM}}, \quad (5.3)$$

$$A_{\text{TE}}C_b^{TE, \Lambda\text{CDM}}, \quad (5.4)$$

$$A_{\text{BL}}C_b^{EB, \text{BL}}, \quad (5.5)$$

$$A_{\text{TT}}C_b^{TT, \Lambda\text{CDM}} + A_{\text{EE}}C_b^{EE, \Lambda\text{CDM}} + A_{\text{TE}}C_b^{TE, \Lambda\text{CDM}} + A_{\text{BL}}C_b^{EB, \text{BL}} \quad (5.6)$$

by minimizing a simple χ^2 function:

$$\chi_{ij, M}^2 = \sum_b \left(\langle C_b^{E_i B_j} \rangle - M_b \right)^2 / V_b^{ij}. \quad (5.7)$$

The mean angular power spectra in Eq. (5.7) are calculated as

$$\langle C_b^{XY} \rangle = \frac{1}{\Delta\ell} \sum_{\ell \in b} \langle C_\ell^{XY} \rangle_{\text{sim}}, \quad (5.8)$$

with variance

$$V_b^{ij} = \frac{1}{f_{\text{sky}} N_{\text{sim}} \Delta\ell^2} \sum_{\ell \in b} \frac{1}{2\ell + 1} \left[\langle C_\ell^{E_i E_i} \rangle_{\text{sim}} \langle C_\ell^{B_j B_j} \rangle_{\text{sim}} + \langle C_\ell^{E_i B_j} \rangle_{\text{sim}}^2 \right]. \quad (5.9)$$

Note the N_{sim}^{-1} factor in Eq. (5.9), since $\chi_{ij,M}^2$ describes a fit to the mean EB angular power spectra and thus V_b^{ij} is the variance of the mean.

In figures 13 and 14, dashed colored lines show the best fit for each model, with the goodness of fit quantified by the reduced χ^2 included on the bottom-left corner of each plot. To get an intuition of the relative importance of each systematic, we also show on the top-left corner of each plot the values of the A_{TT} , A_{EE} , A_{TE} , and A_{BL} amplitudes obtained from the fit to Eq. (5.6). For completeness, the green shaded regions in figures 13, 14, and 15 show the 1σ confidence contours of the EB correlation expected from the α_i^{sys} angles found in figure 11. For every combination of ij bands, these contours are generated by plotting the $C_\ell^{E_i B_j} = (s(4\alpha_j^{\text{sys}})C_\ell^{E_i E_j,0} - s(4\alpha_i^{\text{sys}})C_\ell^{B_i B_j,0}) / (c(4\alpha_i^{\text{sys}}) + c(4\alpha_j^{\text{sys}}))$ spectra produced by the angles found in CMB + N simulations that fall within the 1σ confidence ellipse of the correlation between each α_i^{sys} α_j^{sys} pair.

The fits in figure 13 suggest the presence of a cross-polarization effect leaking E modes into B modes at 100GHz. This kind of systematic is particularly dangerous since our estimator relies on finding a signal resembling $C_\ell^{EE,\Lambda\text{CDM}}$ in the observed EB correlation to determine both birefringence and miscalibration angles. Moreover, the fit to $A_{\text{EE}}C_b^{EE,\Lambda\text{CDM}}$ falls perfectly within the 1σ confidence contours from α_i^{sys} angles, confirming that such a cross-polarization effect is indeed the cause of the $\alpha_{100A}^{\text{sys}}$ and $\alpha_{100B}^{\text{sys}}$ angles found in the simulations.

Although the spread in χ^2/N_{dof} from the fits in figure 14 is smaller than that from figure 13, the fits suggest that beam leakage is the main contribution to the spurious EB correlation seen at those frequencies. Beam leakage has an angular dependence that our estimator cannot reproduce, since it only considers rotations of the observed EE and BB angular power spectra. Nevertheless, the approximate match between the green confidence contours and the mean EB spectra of CMB+N simulations in figure 14 shows how the estimator is trying to accommodate $C_\ell^{EB,\text{BL}}$ as a rotation of $C_\ell^{EE,\Lambda\text{CDM}}$. This limited ability to reproduce the signal from beam leakage leads to the $\alpha_{143A}^{\text{sys}}$, $\alpha_{143B}^{\text{sys}}$, and $\alpha_{217A}^{\text{sys}}$ angles found in the simulations at a lower significance level.

Finding the presence of these cross-polarization and beam leakage effects is important for understanding all the systematics at play in both simulations and, presumably, the real *Planck* data. Nevertheless, note that the α_i^{sys} angles found in CMB+N simulations do not need to agree with the ones found in the data because these simulations do not include the actual (unknown) miscalibration angles present in the data. The α_i^{sys} found here would only match the angles found in the data if the orientation of *Planck*'s polarimeters was perfectly calibrated. In this way, the main conclusion to draw from these results is that, even in the presence of such systematics, our methodology is able to correctly capture their effect within the α_i parameters, leaving the measurement of β not significantly affected by any of them. The $\langle\bar{\alpha}_{\text{sys}}\rangle = -0.009^\circ \pm 0.003^\circ$ angle that we find falls well below the corresponding 0.06° uncertainty that we have on β when simultaneously fitting β and α_i (see figure 8). This observation justifies the decision not to correct the β measurement in Ref. [49] for any of the known systematics.

6 Impact of noise bias

Although cosmic variance limited for the temperature power spectrum, *Planck*'s polarization noise levels are still relatively high [79]. As seen in figure 16, the noise bias in the frequency auto-spectra (e.g., 100×100 full-mission) is high enough to obscure most of the CMB and

foreground EE signal. Such noise-dominated EE can potentially bias β and α_i measurements, since our estimator heavily relies on observed angular power spectra to fit rotation angles and build the covariance matrix. To avoid those biases, frequency auto-spectra were excluded from the analysis of Ref. [49]. Here we quantify the impact of instrumental noise by applying estimators that use information coming from all spectra, only auto-spectra, or only cross-spectra, to $\text{FG}^\alpha + \text{CMB}^{\alpha+\beta} + \text{N}$ simulations.

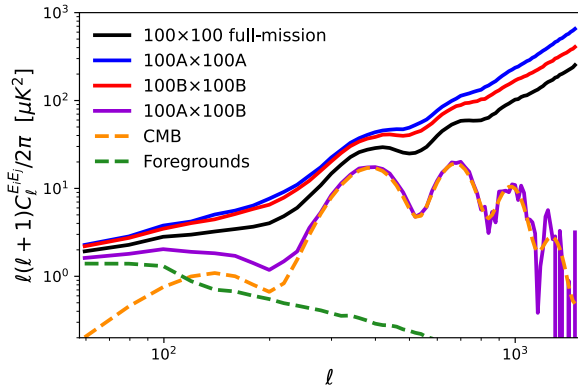


Figure 16: EE angular power spectra from the auto-correlation of NPIPE’s full-mission simulation at 100GHz (black), and 100A (blue) and 100B (red) detector splits, compared to that from the cross-correlation of A and B detector splits (purple). Foreground (green) and CMB (orange) signals are shown for reference. Spectra were calculated with the C0+PS mask and binned from $\ell \in [51, 1490]$ with $\Delta\ell = 20$.

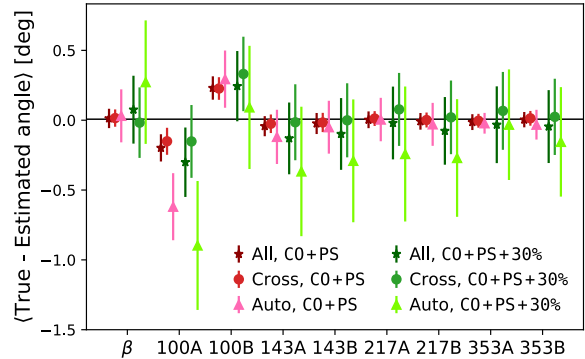


Figure 17: Bias in the estimation of birefringence and polarization angles from $\text{FG}^\alpha + \text{CMB}^{\alpha+\beta} + \text{N}$ simulations with estimators that model the foreground EB correlation (\mathcal{A} free), and that use all (stars), cross-spectra-only (circles), and auto-spectra-only (triangles) information. Uncertainties are calculated as the simulations’ dispersion. Results are shown for only the smallest and largest Galactic masks considered in this work.

Figure 17 shows that measurements derived from auto-spectra-only estimators (light pink and green triangles) lead to higher biases, especially when large Galactic masks are applied. Nevertheless, the higher biases are accompanied by the corresponding increase in the uncertainty, ensuring that the estimates remain compatible with zero within the error bars. When interpreting these results, remember that we expect to recover approximately -0.2° and 0.3° values for α_{100A} and α_{100B} , respectively, because of the systematic effects explained in section 5.

Instrumental noise can be mitigated by cross-correlating different observations of the same signal. *Planck*’s NPIPE [48] data release makes this possible by providing A/B detector splits of their frequency maps, which were built from independent subsets of antennas observing at the same frequency. Using cross-spectra, we are able to avoid the noise bias and recover a signal-dominated observed EE spectrum (100A \times 100B on figure 16) that improves the estimation of both birefringence and polarization angles. In addition, statistical uncertainties are reduced since the likelihood has N_ν times ($N_\nu - 1$ times) more information when all spectra (only cross-spectra) are used [44]. As seen in figure 17, the effect of noise is diluted once cross-spectra are included. To further avoid noise bias, we can exclude auto-spectra from the cross-spectra estimator. With respect to the estimator that includes all correlations (dark red and green stars), this cross-spectra-only estimator (red and green circles) reduces

the mean value obtained with the CO+PS mask by 30%, and that of the CO+PS+30% mask by 60%, while keeping uncertainties compatible within a 5% level.

The superior performance of cross-spectra estimators in noise-dominated experiments like *Planck* was already anticipated in Ref. [60]. Nevertheless, the improvement in polarization noise levels planned for the next generation of CMB experiments will allow for a signal-dominated measurement of E modes without resorting to cross-correlations. Reference [60] showed that, for an experiment such as LiteBIRD [39], auto-spectra-only estimators were more suited for the estimation of miscalibrated polarization angles because of their simpler covariance matrices. We leave the study of the methodology performance in the signal-dominated regime and its application to LiteBIRD for a future work.

7 Conclusions

In this work, we have used realistic simulations of *Planck* data to test the impact that Galactic foreground emission and instrumental systematics have on recent birefringence measurements [13, 46, 49, 59]. To reduce the computational cost of such an extensive simulation study, we have developed a semi-analytical iterative algorithm that simultaneously calculates birefringence and miscalibrated polarization angles within the small-angle approximation. Our simulation study supports the results presented in Ref. [49], confirming and highlighting the importance of accounting for dust EB when simultaneously estimating birefringence and miscalibration angles. It also proves that our methodology is robust, not only against the miscalibration of polarization angles, but also against other systematics like intensity-to-polarization leakage, beam leakage, or cross-polarization effects.

We have demonstrated that a model for Galactic foreground emission is needed to calibrate polarization angles and measure cosmic birefringence at the same time. Thus, having a precise characterization of Galactic foregrounds is the most critical aspect of the analysis. For both the simulation study performed here and the application to *Planck*-HFI data presented in Ref. [49], we adopted the **Commander** sky model as our foreground model. Although **Commander** offers one of the best descriptions of thermal dust emission currently available, it still has its limitations. In particular, **Commander** does not yet provide a signal-dominated template for the foreground EB and it might contain spurious EB correlations through not contemplating the existence of miscalibration angles and the integration of different dust clouds along the line-of-sight in its SED. Our results also lead us to believe that **Commander** might struggle to reproduce dust emission near the center of the Galactic plane. The comparison of simulations and data tells us that the limited signal-to-noise of the template leads to a $\approx 20\%$ underestimation of the uncertainty of the birefringence angle reported in [49]. However, as they are themselves based on the **Commander** sky model, our simulations do not allow us to quantitatively assess the impact that polarized mixing and miscalibration angles have on the foreground model. Therefore, we leave such a study for a future work.

To overcome these obstacles, a self-consistent end-to-end study encompassing component-separation to birefringence estimation is needed. As demonstrated in Ref. [60] using the **B-SeCRET** method [80], it should be possible to derive a new template of polarized foreground emission free of any spurious EB correlation by adding miscalibration angles to the synchrotron and thermal dust SEDs fitted in Bayesian component-separation analyses. Such a self-consistent study would allow us to correctly propagate uncertainties through the whole pipeline and check the consistency of the birefringence and miscalibration angles obtained at all stages: from frequency maps, to component-separation, and the final clean CMB

maps. A better characterization of dust emission beyond the single modified blackbody paradigm [68, 71, 78] and high-precision measurements of the CMB polarization from which to derive a signal-dominated template on the full-sky are also required. We believe that such an analysis will allow for an unbiased and reliable measurement of cosmic birefringence in the future.

Finally, here we have limited ourselves to the study of the high-frequency bands of the *Planck* satellite, where thermal dust emission is the main foreground component. Nevertheless, lower frequency bands could be added to the analysis by including an additional template to describe synchrotron radiation. We will explore that extension of the methodology, and its application to the forecasting of LiteBIRD’s capabilities and to the analysis of *Planck* and WMAP [59] data in future works.

Acknowledgments

This research used resources of the National Energy Research Scientific Computing Center (NERSC), a U.S. Department of Energy Office of Science User Facility operated under Contract No. DE-AC02-05CH11231. Part of the research was carried out at the Jet Propulsion Laboratory, California Institute of Technology, under a contract with the National Aeronautics and Space Administration (80NM0018D0004). PDP acknowledges financial support from the *Formación del Profesorado Universitario* program of the Spanish Ministerio de Ciencia, Innovación y Universidades. EdIH acknowledges financial support from the *Concepción Arenal* program of the Universidad de Cantabria. PDP, EMG, PV, BB, and EdIH thank the Spanish Agencia Estatal de Investigación (AEI, MICIU) for the financial support provided under the projects with references PID2019-110610RB-C21, ESP2017-83921-C2-1-R, and AYA2017-90675-REDC, co-funded with EU FEDER funds, and acknowledge support from Universidad de Cantabria and Consejería de Universidades, Igualdad, Cultura y Deporte del Gobierno de Cantabria via the *Instrumentación y ciencia de datos para sondear la naturaleza del universo* project, as well as from Unidad de Excelencia María de Maeztu (MDM-2017-0765). JRE acknowledges funding from the European Research Council (ERC) under the Horizon 2020 Research and Innovation Program (Grant agreement No. 819478). The work of YM was supported in part by the Japan Society for the Promotion of Science (JSPS) KAKENHI, Grants No. JP20K14497. RS and DS acknowledge the support of the Natural Sciences and Engineering Research Council of Canada. The work of EK was supported in part by JSPS KAKENHI Grant No. JP20H05850 and JP20H05859, and the Deutsche Forschungsgemeinschaft (DFG, German Research Foundation) under Germany’s Excellence Strategy - EXC-2094 - 390783311. The Kavli IPMU is supported by World Premier International Research Center Initiative (WPI), MEXT, Japan. We acknowledge the use of CAMB [81], HEALPix [82], NaMaster [76], emcee [83], corner [84], Matplotlib [85], and Numpy [86].

A Cross-spectra estimator

Starting from Eq. (2.2), we build a maximum likelihood estimator that uses the information from all the frequency cross-spectra to simultaneously calculate β and α_i . In its more general

form, the observed EB correlation across different frequency bands is now the rotation of

$$C_\ell^{E_i B_j, \circ} = \frac{1}{c(4\alpha_i) + c(4\alpha_j)} \left(s(4\alpha_j) C_\ell^{E_i E_j, \circ} - s(4\alpha_i) C_\ell^{B_i B_j, \circ} + 2c(2\alpha_i)c(2\alpha_j) \mathcal{A} C_\ell^{E_i B_j, \text{fg}} \right. \\ \left. + 2s(2\alpha_i)s(2\alpha_j) \mathcal{A} C_\ell^{B_i E_j, \text{fg}} \right) + \frac{s(4\beta)}{2c(2\alpha_i + 2\alpha_j)} \left(C_\ell^{E_i E_j, \Lambda\text{CDM}} - C_\ell^{B_i B_j, \Lambda\text{CDM}} \right). \quad (\text{A.1})$$

Analogously to what was done in section 2, we build a Gaussian likelihood from Eq. (A.1) that, within the small-angle approximation, reads

$$-2 \ln \mathcal{L} \supset \sum_{i,j,p,q} \sum_{\ell} \left[C_\ell^{E_i B_j, \circ} - 2\alpha_j C_\ell^{E_i E_j, \circ} + 2\alpha_i C_\ell^{B_i B_j, \circ} - \mathcal{A} C_\ell^{E_i B_j, \text{fg}} - 2\beta \chi_{ij\ell}^{\Lambda\text{CDM}} \right] \times \\ \mathbf{C}_{ijpq\ell}^{-1} \left[C_\ell^{E_p B_q, \circ} - 2\alpha_q C_\ell^{E_p E_q, \circ} + 2\alpha_p C_\ell^{B_p B_q, \circ} - \mathcal{A} C_\ell^{E_p B_q, \text{fg}} - 2\beta \chi_{pq\ell}^{\Lambda\text{CDM}} \right]. \quad (\text{A.2})$$

In this case, the $\mathbf{C}_{ijpq\ell}$ covariance matrix has $N_\nu^2 N_\ell \times N_\nu^2 N_\ell$ elements. Under the approximation in Eq. (2.7), the $\mathbf{C}_{ijpq\ell}$ covariance matrix in Eq. (A.2) can be divided into terms that depend only on the observed, foreground, and CMB spectra, and on their cross-correlations:

$$\mathbf{C}_{ijpq\ell} = \frac{1}{(2\ell + 1) f_{\text{sky}}} \left[\mathbf{C}_{ijpq\ell}^{\circ} + \mathbf{C}_{ijpq\ell}^{\text{CMB}} + \mathbf{C}_{ijpq\ell}^{\text{fg}} + \mathbf{C}_{ijpq\ell}^{\text{CMB}^* \circ} + \mathbf{C}_{ijpq\ell}^{\text{fg}^* \circ} \right]. \quad (\text{A.3})$$

Expanding $C_\ell^{X^{\text{CMB}Y^{\circ}}}$ angular power spectra like $C_\ell^{X^{\text{CMB}Y^{\circ}}} = \frac{1}{2\ell+1} \sum_{m=-\ell}^{\ell} X_{\ell m}^{\text{CMB}Y^{\circ}} X_{\ell m}^{\circ}$, and acknowledging that the spherical harmonic coefficients of the observed signal are a rotation of the CMB and foreground ones as shown in Eq. (2.1), the contribution of all CMB-related terms is reduced to

$$\mathbf{C}_{ijpq\ell}^{\text{CMB}} + \mathbf{C}_{ijpq\ell}^{\text{CMB}^* \circ} = -\frac{s^2(4\beta) b_\ell^i b_\ell^j b_\ell^p b_\ell^q \omega_{\text{pix}, \ell}^4}{2c(2\alpha_i + 2\alpha_j)c(2\alpha_p + 2\alpha_q)} \left[\left(C_\ell^{EE, \Lambda\text{CDM}} \right)^2 + \left(C_\ell^{BB, \Lambda\text{CDM}} \right)^2 \right], \quad (\text{A.4})$$

where $C_\ell^{EE, \Lambda\text{CDM}}$ and $C_\ell^{BB, \Lambda\text{CDM}}$ are the theoretical angular power spectra predicted by ΛCDM , and the combination of ij frequency bands is specified through the different beam and pixel window functions, b_ℓ^i and $\omega_{\text{pix}, \ell}$, respectively.

The terms depending on the observed and foreground spectra are calculated as follows:

$$\mathbf{C}_{ijpq\ell}^{\circ} = C_\ell^{E_i^{\circ} E_p^{\circ}} C_\ell^{B_j^{\circ} B_q^{\circ}} + C_\ell^{E_i^{\circ} B_q^{\circ}} C_\ell^{B_j^{\circ} E_p^{\circ}} \\ + \frac{s(4\alpha_p)}{c(4\alpha_p) + c(4\alpha_q)} \left(C_\ell^{E_i^{\circ} B_p^{\circ}} C_\ell^{B_j^{\circ} B_q^{\circ}} + C_\ell^{E_i^{\circ} B_q^{\circ}} C_\ell^{B_j^{\circ} B_p^{\circ}} \right) \\ - \frac{s(4\alpha_q)}{c(4\alpha_p) + c(4\alpha_q)} \left(C_\ell^{E_i^{\circ} E_p^{\circ}} C_\ell^{B_j^{\circ} E_q^{\circ}} + C_\ell^{E_i^{\circ} E_q^{\circ}} C_\ell^{B_j^{\circ} E_p^{\circ}} \right) \\ + \frac{s(4\alpha_i)}{c(4\alpha_i) + c(4\alpha_j)} \left(C_\ell^{B_i^{\circ} E_p^{\circ}} C_\ell^{B_j^{\circ} B_q^{\circ}} + C_\ell^{B_i^{\circ} B_q^{\circ}} C_\ell^{B_j^{\circ} E_p^{\circ}} \right) \\ - \frac{s(4\alpha_j)}{c(4\alpha_i) + c(4\alpha_j)} \left(C_\ell^{E_i^{\circ} E_p^{\circ}} C_\ell^{E_j^{\circ} B_q^{\circ}} + C_\ell^{E_i^{\circ} B_q^{\circ}} C_\ell^{E_j^{\circ} E_p^{\circ}} \right) \\ + \frac{s(4\alpha_j)s(4\alpha_q)}{[c(4\alpha_i) + c(4\alpha_j)][c(4\alpha_p) + c(4\alpha_q)]} \left(C_\ell^{E_i^{\circ} E_p^{\circ}} C_\ell^{E_j^{\circ} E_q^{\circ}} + C_\ell^{E_i^{\circ} E_q^{\circ}} C_\ell^{E_j^{\circ} E_p^{\circ}} \right) \\ + \frac{s(4\alpha_i)s(4\alpha_p)}{[c(4\alpha_i) + c(4\alpha_j)][c(4\alpha_p) + c(4\alpha_q)]} \left(C_\ell^{B_i^{\circ} B_p^{\circ}} C_\ell^{B_j^{\circ} B_q^{\circ}} + C_\ell^{B_i^{\circ} B_q^{\circ}} C_\ell^{B_j^{\circ} B_p^{\circ}} \right)$$

$$\begin{aligned}
& - \frac{s(4\alpha_j)s(4\alpha_p)}{[c(4\alpha_i) + c(4\alpha_j)][c(4\alpha_p) + c(4\alpha_q)]} \left(C_\ell^{E_i^\circ B_p^\circ} C_\ell^{E_j^\circ B_q^\circ} + C_\ell^{E_i^\circ B_q^\circ} C_\ell^{E_j^\circ B_p^\circ} \right) \\
& - \frac{s(4\alpha_i)s(4\alpha_q)}{[c(4\alpha_i) + c(4\alpha_j)][c(4\alpha_p) + c(4\alpha_q)]} \left(C_\ell^{B_i^\circ E_p^\circ} C_\ell^{B_j^\circ E_q^\circ} + C_\ell^{B_i^\circ E_q^\circ} C_\ell^{B_j^\circ E_p^\circ} \right) \tag{A.5}
\end{aligned}$$

and

$$\begin{aligned}
\mathbf{C}_{ijpq\ell}^{\text{fg}} = & \frac{4\mathcal{A}^2}{[c(4\alpha_i) + c(4\alpha_j)][c(4\alpha_p) + c(4\alpha_q)]} \left[\right. \\
& c(2\alpha_i)c(2\alpha_j)c(2\alpha_p)c(2\alpha_q) \left(C_\ell^{E_i^{\text{fg}} E_p^{\text{fg}}} C_\ell^{B_j^{\text{fg}} B_q^{\text{fg}}} + C_\ell^{E_i^{\text{fg}} B_q^{\text{fg}}} C_\ell^{B_j^{\text{fg}} E_p^{\text{fg}}} \right) \\
& + c(2\alpha_i)c(2\alpha_j)s(2\alpha_p)s(2\alpha_q) \left(C_\ell^{E_i^{\text{fg}} B_p^{\text{fg}}} C_\ell^{B_j^{\text{fg}} E_q^{\text{fg}}} + C_\ell^{E_i^{\text{fg}} E_q^{\text{fg}}} C_\ell^{B_j^{\text{fg}} B_p^{\text{fg}}} \right) \\
& + s(2\alpha_i)s(2\alpha_j)c(2\alpha_p)c(2\alpha_q) \left(C_\ell^{B_i^{\text{fg}} E_p^{\text{fg}}} C_\ell^{E_j^{\text{fg}} B_q^{\text{fg}}} + C_\ell^{B_i^{\text{fg}} B_q^{\text{fg}}} C_\ell^{E_j^{\text{fg}} E_p^{\text{fg}}} \right) \\
& \left. + s(2\alpha_i)s(2\alpha_j)s(2\alpha_p)s(2\alpha_q) \left(C_\ell^{B_i^{\text{fg}} B_p^{\text{fg}}} C_\ell^{E_j^{\text{fg}} E_q^{\text{fg}}} + C_\ell^{B_i^{\text{fg}} E_q^{\text{fg}}} C_\ell^{E_j^{\text{fg}} B_p^{\text{fg}}} \right) \right]. \tag{A.6}
\end{aligned}$$

Finally, the cross-correlation between the observed and foreground signals is given as

$$\begin{aligned}
\mathbf{C}_{ijpq\ell}^{\text{fg*o}} = & - \frac{2\mathcal{A}c(2\alpha_i)c(2\alpha_j)}{c(4\alpha_i) + c(4\alpha_j)} \left(C_\ell^{E_i^{\text{fg}} E_p^\circ} C_\ell^{B_j^{\text{fg}} B_q^\circ} + C_\ell^{E_i^{\text{fg}} B_q^\circ} C_\ell^{B_j^{\text{fg}} E_p^\circ} \right) \\
& - \frac{2\mathcal{A}c(2\alpha_p)c(2\alpha_q)}{c(4\alpha_p) + c(4\alpha_q)} \left(C_\ell^{E_i^\circ E_p^{\text{fg}}} C_\ell^{B_j^\circ B_q^{\text{fg}}} + C_\ell^{E_i^\circ B_q^{\text{fg}}} C_\ell^{B_j^\circ E_p^{\text{fg}}} \right) \\
& - \frac{2\mathcal{A}s(2\alpha_i)s(2\alpha_j)}{c(4\alpha_i) + c(4\alpha_j)} \left(C_\ell^{B_i^{\text{fg}} E_p^\circ} C_\ell^{E_j^{\text{fg}} B_q^\circ} + C_\ell^{B_i^{\text{fg}} B_q^\circ} C_\ell^{E_j^{\text{fg}} E_p^\circ} \right) \\
& - \frac{2\mathcal{A}s(2\alpha_p)s(2\alpha_q)}{c(4\alpha_p) + c(4\alpha_q)} \left(C_\ell^{E_i^\circ B_p^{\text{fg}}} C_\ell^{B_j^\circ E_q^{\text{fg}}} + C_\ell^{E_i^\circ E_q^{\text{fg}}} C_\ell^{B_j^\circ B_p^{\text{fg}}} \right) \\
& + \frac{2\mathcal{A}c(2\alpha_p)c(2\alpha_q)s(4\alpha_j)}{[c(4\alpha_i) + c(4\alpha_j)][c(4\alpha_p) + c(4\alpha_q)]} \left(C_\ell^{E_i^\circ E_p^{\text{fg}}} C_\ell^{E_j^\circ B_q^{\text{fg}}} + C_\ell^{E_i^\circ B_q^{\text{fg}}} C_\ell^{E_j^\circ E_p^{\text{fg}}} \right) \\
& + \frac{2\mathcal{A}c(2\alpha_i)c(2\alpha_j)s(4\alpha_q)}{[c(4\alpha_i) + c(4\alpha_j)][c(4\alpha_p) + c(4\alpha_q)]} \left(C_\ell^{E_i^{\text{fg}} E_p^\circ} C_\ell^{B_j^{\text{fg}} E_q^\circ} + C_\ell^{E_i^{\text{fg}} E_q^\circ} C_\ell^{B_j^{\text{fg}} E_p^\circ} \right) \\
& + \frac{2\mathcal{A}s(2\alpha_p)s(2\alpha_q)s(4\alpha_j)}{[c(4\alpha_i) + c(4\alpha_j)][c(4\alpha_p) + c(4\alpha_q)]} \left(C_\ell^{E_i^\circ B_p^{\text{fg}}} C_\ell^{E_j^\circ E_q^{\text{fg}}} + C_\ell^{E_i^\circ E_q^{\text{fg}}} C_\ell^{E_j^\circ B_p^{\text{fg}}} \right) \\
& + \frac{2\mathcal{A}s(2\alpha_i)s(2\alpha_j)s(4\alpha_q)}{[c(4\alpha_i) + c(4\alpha_j)][c(4\alpha_p) + c(4\alpha_q)]} \left(C_\ell^{B_i^{\text{fg}} E_p^\circ} C_\ell^{E_j^{\text{fg}} E_q^\circ} + C_\ell^{B_i^{\text{fg}} E_q^\circ} C_\ell^{E_j^{\text{fg}} E_p^\circ} \right) \\
& - \frac{2\mathcal{A}c(2\alpha_p)c(2\alpha_q)s(4\alpha_i)}{[c(4\alpha_i) + c(4\alpha_j)][c(4\alpha_p) + c(4\alpha_q)]} \left(C_\ell^{B_i^\circ E_p^{\text{fg}}} C_\ell^{B_j^\circ B_q^{\text{fg}}} + C_\ell^{B_i^\circ B_q^{\text{fg}}} C_\ell^{B_j^\circ E_p^{\text{fg}}} \right) \\
& - \frac{2\mathcal{A}c(2\alpha_i)c(2\alpha_j)s(4\alpha_p)}{[c(4\alpha_i) + c(4\alpha_j)][c(4\alpha_p) + c(4\alpha_q)]} \left(C_\ell^{E_i^{\text{fg}} B_p^\circ} C_\ell^{B_j^{\text{fg}} B_q^\circ} + C_\ell^{E_i^{\text{fg}} B_q^\circ} C_\ell^{B_j^{\text{fg}} B_p^\circ} \right) \\
& - \frac{2\mathcal{A}s(2\alpha_p)s(2\alpha_q)s(4\alpha_i)}{[c(4\alpha_i) + c(4\alpha_j)][c(4\alpha_p) + c(4\alpha_q)]} \left(C_\ell^{B_i^\circ B_p^{\text{fg}}} C_\ell^{B_j^\circ E_q^{\text{fg}}} + C_\ell^{B_i^\circ E_q^{\text{fg}}} C_\ell^{B_j^\circ B_p^{\text{fg}}} \right)
\end{aligned}$$

$$-\frac{2As(2\alpha_i)s(2\alpha_j)s(4\alpha_p)}{[c(4\alpha_i) + c(4\alpha_j)][c(4\alpha_p) + c(4\alpha_q)]} \left(C_\ell^{B_i^{fg} B_p^o} C_\ell^{E_j^{fg} B_q^o} + C_\ell^{B_i^{fg} B_q^o} C_\ell^{E_j^{fg} B_p^o} \right). \quad (\text{A.7})$$

After binning both the angular power spectra and the covariance matrix, the minimization of Eq. (A.2) leads to a linear system with the same structure as that of Eq. (2.10), but with \mathbf{A}_{mn} elements that are now

$$\Xi = \sum_{i,j,p,q} \sum_b C_b^{E_i B_j, fg} \mathbf{C}_{ijpq}^{-1} C_b^{E_p B_q, fg}, \quad (\text{A.8})$$

$$Z = 2 \sum_{i,j,p,q} \sum_b C_b^{E_i B_j, fg} \mathbf{C}_{ijpq}^{-1} \chi_{pq}^{\Lambda\text{CDM}}, \quad (\text{A.9})$$

$$\Theta = 4 \sum_{i,j,p,q} \sum_b \chi_{ij}^{\Lambda\text{CDM}} \mathbf{C}_{ijpq}^{-1} \chi_{pq}^{\Lambda\text{CDM}}, \quad (\text{A.10})$$

$$K_m = 2 \sum_{i,p,q} \sum_b \left[C_b^{E_i E_m, o} \mathbf{C}_{impq}^{-1} C_b^{E_p B_q, fg} - C_b^{B_m B_i, o} \mathbf{C}_{mipq}^{-1} C_b^{E_p B_q, fg} \right], \quad (\text{A.11})$$

$$T_m = 4 \sum_{i,p,q} \sum_b \left[C_b^{E_i E_m, o} \mathbf{C}_{impq}^{-1} \chi_{pq}^{\Lambda\text{CDM}} - C_b^{B_m B_i, o} \mathbf{C}_{mipq}^{-1} \chi_{pq}^{\Lambda\text{CDM}} \right], \quad (\text{A.12})$$

$$\begin{aligned} \Omega_{mn} = & 4 \sum_{i,j} \sum_b \left[C_b^{E_i E_n, o} \mathbf{C}_{injm}^{-1} C_b^{E_j E_m, o} + C_b^{B_n B_i, o} \mathbf{C}_{nimj}^{-1} C_b^{B_m B_j, o} \right] \\ & - 4 \sum_{i,j} \sum_b \left[C_b^{B_n B_i, o} \mathbf{C}_{nijm}^{-1} C_b^{E_j E_m, o} + C_b^{B_m B_j, o} \mathbf{C}_{mjib}^{-1} C_b^{E_i E_n, o} \right]. \end{aligned} \quad (\text{A.13})$$

and \mathbf{b}_m terms

$$\xi = \sum_{i,j,p,q} \sum_b C_b^{E_i B_j, fg} \mathbf{C}_{ijpq}^{-1} C_b^{E_p B_q, o}, \quad (\text{A.14})$$

$$\theta = 2 \sum_{i,j,p,q} \sum_b C_b^{E_i B_j, o} \mathbf{C}_{ijpq}^{-1} \chi_{pq}^{\Lambda\text{CDM}}, \quad (\text{A.15})$$

$$\omega_m = 2 \sum_{i,p,q} \sum_b \left[C_b^{E_i E_m, o} \mathbf{C}_{impq}^{-1} C_b^{E_p B_q, o} - C_b^{B_m B_i, o} \mathbf{C}_{mipq}^{-1} C_b^{E_p B_q, o} \right], \quad (\text{A.16})$$

Once again, the uncertainty in the estimation of the $\mathbf{x}_i = (\mathcal{A}, \beta, \alpha_i)$ parameters is calculated within the Fisher matrix approximation as $\mathbf{C}_{mn}^{-1} = -\frac{\partial^2 \ln \mathcal{L}}{\partial \mathbf{x}_m \partial \mathbf{x}_n} = \mathbf{A}_{mn}$.

By exploiting the cross-correlation of different frequency bands, the cross-spectra estimator is statistically more powerful than the auto-spectra-only estimator defined in section 2, due to the sheer increase of available information (from N_ν to N_ν^2 equations) [44]. It is also more robust against instrumental noise bias. On the other hand, the greater complexity of the cross-spectra estimator's covariance matrix makes it more prone to suffer from the numerical instabilities that arise from calculating the covariance matrix from observed spectra rather than from theoretical models. As explored in Ref. [60], such numerical instabilities are mitigated by optimizing the range of multipoles used in the analysis, smoothing the spectra, or binning the covariance matrix.

Note that we can avoid the noise bias contained in frequency auto-spectra with a minimal loss of information if we build an estimator that exclusively uses cross-spectra by explicitly leaving auto-spectra out of the summations in the elements of the linear system. In practice, this is done by changing $\sum_{i,j,p,q} \rightarrow \sum_{i,j \neq i} \sum_{p,q \neq p}$ in Eqs. (A.8), (A.9), (A.10), (A.14), and

(A.15), $\sum_{i,p,q} \rightarrow \sum_{i \neq m} \sum_{p,q \neq p}$ in Eqs. (A.11), (A.12), and (A.16), and $\sum_{i,j} \rightarrow \sum_{i \neq n} \sum_{j \neq m}$ in Eq. (A.13). For this cross-spectra-only estimator, the size of the covariance matrix is reduced to $N_\nu(N_\nu - 1)N_\ell \times N_\nu(N_\nu - 1)N_\ell$.

B Comparison with MCMC sampling

Here, we briefly compare our semi-analytical algorithm with its counterpart MCMC implementation. By comparing them with the posterior distributions obtained from the MCMC sampling of the full likelihood, figure 19 shows that our algorithm is correctly finding the maximum-likelihood solutions and marginalized Fisher uncertainties for all parameters. Those results validate both our iterative approach and the use of the small-angle approximation.

As discussed in section 2, the likelihood defined for our estimator should include the $\ln |\mathbf{C}|$ term to ensure that the change in the likelihood’s normalization as the free parameters in the covariance matrix vary during the MCMC sampling is taken into account. Therefore, not including the log-determinant can lead to biased posterior distributions. Figure 18 illustrates this effect by showing the maximum-likelihood solutions obtained when including (blue circles) or excluding (orange circles) $\ln |\mathbf{C}|$ from the likelihood, for both the case where foreground EB is ignored (left panel) or accounted for (right panel). The biases produced by ignoring $\ln |\mathbf{C}|$ are more important for smaller sky fractions, and seem to diminish when a template for foreground emission is provided. In both cases, our algorithm yields values (red triangles) that are compatible with those obtained when including $\ln |\mathbf{C}|$, confirming that our iterative approach also accounts for the change in the likelihood’s normalization. The uncertainties derived from our algorithm and the MCMC sampling are compatible within a 1% level for C0+PS and C0+PS+10\% masks, and within 15% for the C0+PS+30\% mask. The latter discrepancy is of the same order of magnitude as the discrepancy seen between the uncertainties derived from Fisher and the simulations’ dispersion in section 4. This suggests that, for large Galactic masks, the Fisher approximation might not be enough to correctly describe posterior distributions.

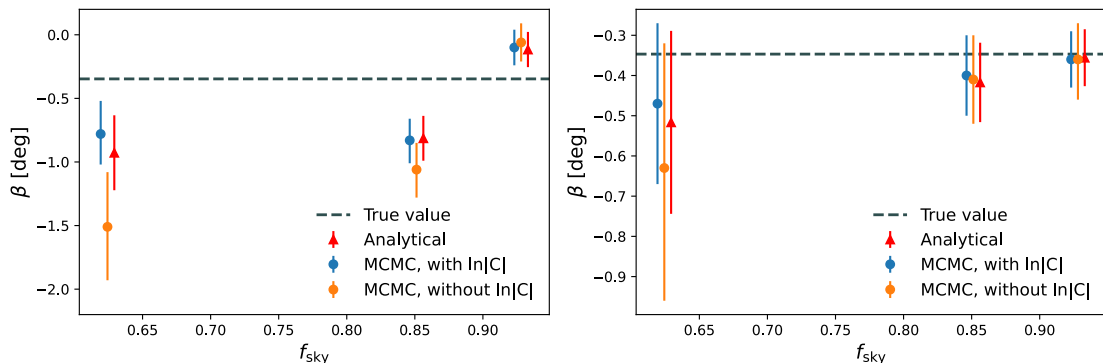


Figure 18: Maximum-likelihood solutions recovered when sampling the full likelihood with MCMC implementations that include (blue circles) or exclude (orange circles) the log-determinant term, compared to those obtained with our semi-analytical algorithm (red triangles). Results on the left correspond to the analysis of one example $\text{FG}^\alpha + \text{CMB}^{\alpha+\beta} + \text{N}$ simulation with $\beta = -0.35^\circ$ when the foreground EB is ignored, and those on the right to the analysis of the same simulation when a foreground template is provided.

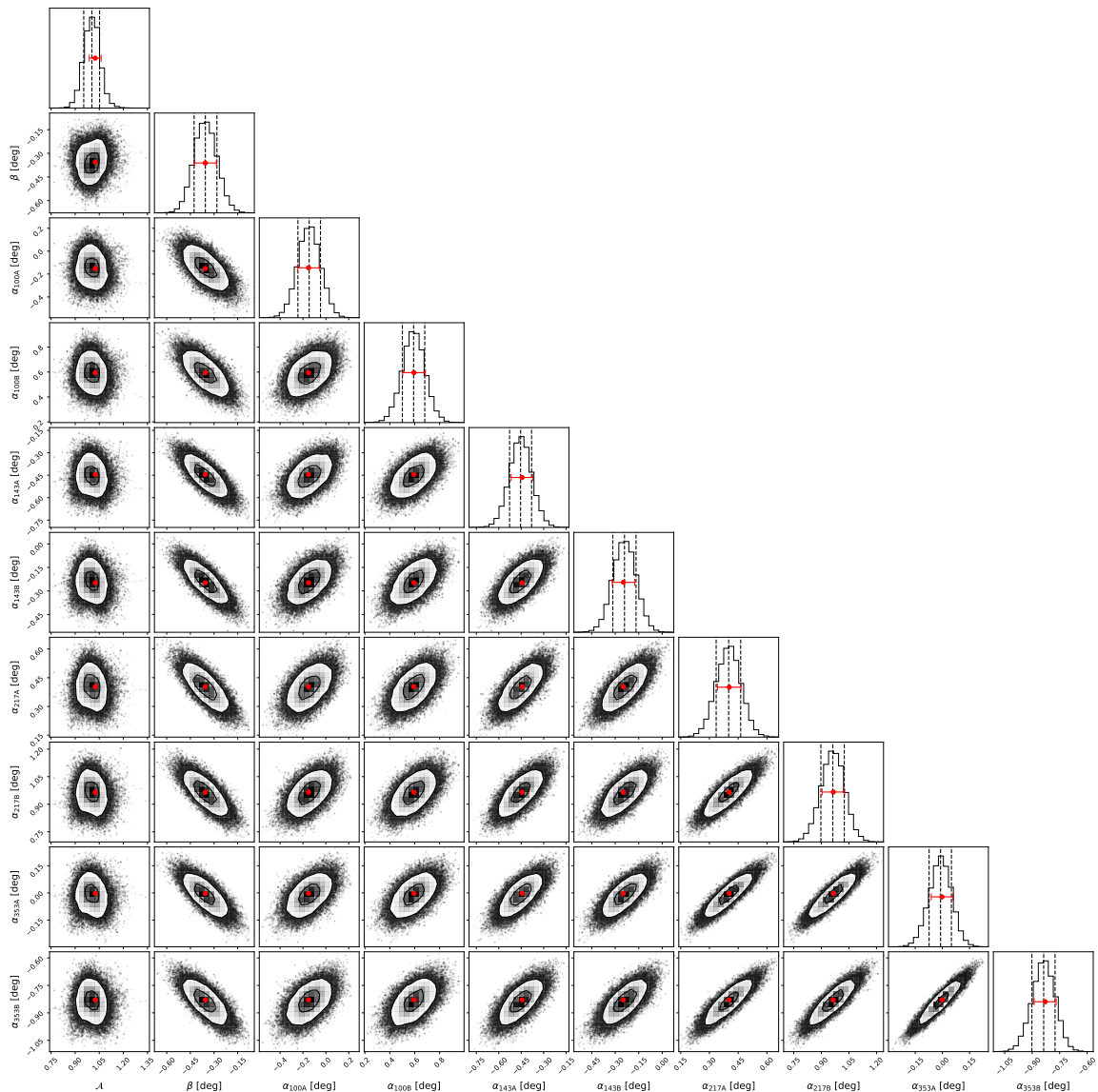


Figure 19: Posterior distributions obtained from the analysis of one example $\text{FG}^\alpha + \text{CMB}^{\alpha+\beta} + \text{N}$ simulation using the CO+PS mask. We sample the full likelihood with an MCMC implementation that includes the log-determinant term and corrects for the foreground EB by providing a template. Overlaid in red are the maximum-likelihood solutions and marginalized Fisher uncertainties calculated with our semi-analytical algorithm.

In terms of computational resources and speed, our semi-analytical algorithm is far superior to the MCMC implementation. Taking the 8 detector splits of *Planck* HFI as a benchmark, and using 60 walkers, running the MCMC sampler parallelized over 64 cores at Cori Haswell⁹ nodes on NERSC takes approximately 4.2s per iteration when the foreground EB contribution is ignored, and 12.9s per iteration when a foreground template is provided.

⁹Cori Haswell nodes have 64 Intel Xeon processors with a 2.3GHz clock rate and a total memory of 128GB per node.

A minimum of around 2500 iterations are needed to obtain fully converged chains, taking from 3 to 9 hours of computation time. In contrast, the semi-analytical algorithm written in plain Python runs on one Cori Haswell core in approximately 7s when the foreground EB contribution is ignored, and 12s when a foreground template is provided. In this sense, our algorithm could be run on any laptop with enough memory to support the volume of data corresponding to the covariance matrix for a given number of frequency bands.

C Calculation of the covariance matrix

Here, we offer a detailed calculation of the covariance matrix presented in section 2 for the frequency auto-spectra estimator. We followed the same procedure to calculate the covariance matrix of the cross-spectra estimator presented in appendix A. In Eq. (2.6), covariance elements are calculated from the observed angular power spectra as well as the models for both foreground and CMB signals. Therefore, once all the products are expanded, the covariance can be divided into terms that depend only on the observed, foreground, and CMB spectra, and on their cross-correlations:

$$\mathbf{C}_{ij\ell} = \frac{1}{(2\ell + 1)f_{\text{sky}}} \left[\mathbf{C}_{ij\ell}^{\circ} + \mathbf{C}_{ij\ell}^{\text{CMB}} + \mathbf{C}_{ij\ell}^{\text{fg}} + \mathbf{C}_{ij\ell}^{\text{CMB*o}} + \mathbf{C}_{ij\ell}^{\text{fg*o}} \right], \quad (\text{C.1})$$

where we have already assumed that correlations between the foreground and CMB signals are negligible¹⁰ ($\mathbf{C}_{ij\ell}^{\text{CMB*fg}} = 0$), and included the sky fraction factor f_{sky} to account for partial sky coverage.

Applying Eq. (2.7), $\mathbf{C}_{ij\ell}^{\circ}$ and $\mathbf{C}_{ij\ell}^{\text{fg}}$ terms are calculated as follows:

$$\begin{aligned} \mathbf{C}_{ij\ell}^{\circ} &= C_{\ell}^{E_i^{\circ} E_j^{\circ}} C_{\ell}^{B_i^{\circ} B_j^{\circ}} + C_{\ell}^{E_i^{\circ} B_j^{\circ}} C_{\ell}^{B_i^{\circ} E_j^{\circ}} \\ &+ t(4\alpha_j) \left[C_{\ell}^{E_i^{\circ} B_j^{\circ}} C_{\ell}^{B_i^{\circ} B_j^{\circ}} - C_{\ell}^{E_i^{\circ} E_j^{\circ}} C_{\ell}^{B_i^{\circ} E_j^{\circ}} \right] \\ &+ t(4\alpha_i) \left[C_{\ell}^{B_i^{\circ} E_j^{\circ}} C_{\ell}^{B_i^{\circ} B_j^{\circ}} - C_{\ell}^{E_i^{\circ} E_j^{\circ}} C_{\ell}^{E_i^{\circ} B_j^{\circ}} \right] \\ &+ \frac{t(4\alpha_i)t(4\alpha_j)}{2} \left[\left(C_{\ell}^{E_i^{\circ} E_j^{\circ}} \right)^2 + \left(C_{\ell}^{B_i^{\circ} B_j^{\circ}} \right)^2 - \left(C_{\ell}^{E_i^{\circ} B_j^{\circ}} \right)^2 - \left(C_{\ell}^{B_i^{\circ} E_j^{\circ}} \right)^2 \right] \end{aligned} \quad (\text{C.2})$$

and

$$\mathbf{C}_{ij\ell}^{\text{fg}} = \frac{\mathcal{A}^2}{c(4\alpha_i)c(4\alpha_j)} \left[C_{\ell}^{E_i^{\text{fg}} E_j^{\text{fg}}} C_{\ell}^{B_i^{\text{fg}} B_j^{\text{fg}}} + C_{\ell}^{E_i^{\text{fg}} B_j^{\text{fg}}} C_{\ell}^{B_i^{\text{fg}} E_j^{\text{fg}}} \right]. \quad (\text{C.3})$$

The cross-correlation between the observed signal and the foreground model is given as

$$\begin{aligned} \mathbf{C}_{ij\ell}^{\text{fg*o}} &= -\frac{\mathcal{A}}{c(4\alpha_i)} \left[C_{\ell}^{E_i^{\text{fg}} E_j^{\circ}} C_{\ell}^{B_i^{\text{fg}} B_j^{\circ}} + C_{\ell}^{B_i^{\text{fg}} E_j^{\circ}} C_{\ell}^{E_i^{\text{fg}} B_j^{\circ}} \right] \\ &- \frac{\mathcal{A}}{c(4\alpha_j)} \left[C_{\ell}^{E_i^{\circ} E_j^{\text{fg}}} C_{\ell}^{B_i^{\circ} B_j^{\text{fg}}} + C_{\ell}^{E_i^{\circ} B_j^{\text{fg}}} C_{\ell}^{B_i^{\circ} E_j^{\text{fg}}} \right] \\ &+ \frac{\mathcal{A}t(4\alpha_j)}{c(4\alpha_i)} \left[C_{\ell}^{E_i^{\text{fg}} E_j^{\circ}} C_{\ell}^{B_i^{\text{fg}} E_j^{\circ}} - C_{\ell}^{E_i^{\text{fg}} B_j^{\circ}} C_{\ell}^{B_i^{\text{fg}} B_j^{\circ}} \right] \\ &+ \frac{\mathcal{A}t(4\alpha_i)}{c(4\alpha_j)} \left[C_{\ell}^{E_i^{\circ} E_j^{\text{fg}}} C_{\ell}^{E_i^{\circ} B_j^{\text{fg}}} - C_{\ell}^{B_i^{\circ} E_j^{\text{fg}}} C_{\ell}^{B_i^{\circ} B_j^{\text{fg}}} \right]. \end{aligned} \quad (\text{C.4})$$

¹⁰Although chance correlations between foreground and CMB signals can be important on a realization-by-realization basis, they are subdominant at the angular scales of interest for this work ($\ell > 50$).

If we had a theoretical model for the foreground angular power spectra, or accepted the **Commander** sky model as an exact representation of the polarized foreground emission on the sky, we could further expand the $C_\ell^{X^{\text{fg}}Y^{\text{o}}}$ terms in Eq. (C.4) by acknowledging that the spherical harmonic coefficients of the observed signal are a rotation of the CMB and foreground ones (see Eq. (2.1)). Therefore, when calculating $C_\ell^{X^{\text{fg}}Y^{\text{o}}} = (2\ell + 1)^{-1} \sum_{m=-\ell}^{\ell} X_{\ell m}^{\text{fg}} Y_{\ell m}^{\text{o}*}$ for any given pair of frequency bands, we will obtain a rotation of $C_\ell^{E^{\text{fg}}E^{\text{fg}}}$, $C_\ell^{E^{\text{fg}}B^{\text{fg}}}$, and $C_\ell^{B^{\text{fg}}B^{\text{fg}}}$. Instead, as we are treating **Commander** as an approximate model, in this work we calculate the $C_\ell^{X^{\text{fg}}Y^{\text{o}}}$ correlations between the observed maps and **Commander** templates to account for any possible mismodeling of the foreground emission.

On the other hand, for the CMB we do expand the corresponding $C_\ell^{X^{\text{CMB}}Y^{\text{o}}}$ terms. In that case, the contribution from CMB-related terms to the covariance is

$$\mathbf{C}_{ij\ell}^{\text{CMB}} = \frac{s^2(4\beta)}{2c(4\alpha_i)c(4\alpha_j)} \left(b_\ell^i b_\ell^j\right)^2 \omega_{\text{pix},\ell}^4 \left[\left(C_\ell^{EE,\Lambda\text{CDM}}\right)^2 + \left(C_\ell^{BB,\Lambda\text{CDM}}\right)^2 \right], \quad (\text{C.5})$$

$$\mathbf{C}_{ij\ell}^{\text{CMB}^*\text{o}} = -\frac{s^2(4\beta)}{c(4\alpha_i)c(4\alpha_j)} \left(b_\ell^i b_\ell^j\right)^2 \omega_{\text{pix},\ell}^4 \left[\left(C_\ell^{EE,\Lambda\text{CDM}}\right)^2 + \left(C_\ell^{BB,\Lambda\text{CDM}}\right)^2 \right], \quad (\text{C.6})$$

where $C_\ell^{EE,\Lambda\text{CDM}}$ and $C_\ell^{BB,\Lambda\text{CDM}}$ are the theoretical angular power spectra predicted by ΛCDM , and the combination of ij frequency bands is specified through the different beam and pixel window functions, b_ℓ^i and $\omega_{\text{pix},\ell}$, respectively.

Note that the covariance matrix is a block matrix composed of $N_\nu \times N_\nu$ diagonal $N_\ell \times N_\ell$ boxes since we are not considering ℓ -to- ℓ' correlations. Hence, our algorithm can be optimized by reordering the $\mathbf{C}_{ij\ell\ell'}$ terms of the covariance into $N_\ell \times N_\ell$ boxes of $N_\nu \times N_\nu$ elements to form a block diagonal matrix whose inverse is calculated by independently inverting each of its blocks. This leads to a faster implementation, since inverting $N_\ell N_\nu \times N_\nu N_\ell$ matrices is faster than inverting one big $N_\nu N_\ell \times N_\nu N_\ell$ matrix, especially when dealing with a large number of frequency bands.

D Modeling Galactic foregrounds in the covariance matrix

In section 4, we saw that the statistical uncertainties in the estimation of β and α_i decreased when the foreground EB was included in the model ($\mathcal{A} \neq 0$). Although counter-intuitive at first, here we will explain why the inclusion of a template for Galactic foreground emission in the covariance matrix leads to a reduction of the total covariance that produces those smaller uncertainties. For simplicity, we will perform these calculations for the frequency auto-spectra estimator.

To determine the role of foregrounds in the covariance matrix, we can assume that our foreground template is a faithful representation of the foreground emission in the sky and expand the $C_\ell^{X^{\text{fg}}Y^{\text{o}}}$ terms in Eq. (C.4) as a rotation of $C_\ell^{E^{\text{fg}}E^{\text{fg}}}$, $C_\ell^{E^{\text{fg}}B^{\text{fg}}}$, and $C_\ell^{B^{\text{fg}}B^{\text{fg}}}$. Under these conditions, the contribution of the foreground template to the covariance is

$$\mathbf{C}_{ij\ell}^{\text{fg}} = \frac{\mathcal{A}^2}{c(4\alpha_i)c(4\alpha_j)} \left[C_\ell^{E_i E_j, \text{fg}} C_\ell^{B_i B_j, \text{fg}} + C_\ell^{E_i B_j, \text{fg}} C_\ell^{B_i E_j, \text{fg}} \right], \quad (\text{D.1})$$

$$\mathbf{C}_{ij\ell}^{\text{fg}^*\text{o}} = -\frac{2\mathcal{A}}{c(4\alpha_i)c(4\alpha_j)} \left[C_\ell^{E_i E_j, \text{fg}} C_\ell^{B_i B_j, \text{fg}} + C_\ell^{E_i B_j, \text{fg}} C_\ell^{B_i E_j, \text{fg}} \right]. \quad (\text{D.2})$$

From these terms alone we can already see that if the template offers a good enough representation of the foreground emission in the sky, then $\mathcal{A} \approx 1$, and $\mathbf{C}_{ij\ell}^{\text{fg}} + \mathbf{C}_{ij\ell}^{\text{fg*o}}$ becomes a negative contribution to the total covariance.

We can also expand the $C_\ell^{X^\circ Y^\circ}$ angular power spectra in Eq. (C.2) by explicitly calculating the correlations between the rotated foreground and CMB components, as written in Eq. (2.1). With that we obtain

$$\begin{aligned}
\mathbf{C}_{ij\ell}^{\text{o}} = & \frac{1}{c(4\alpha_i)c(4\alpha_j)} \left[C_\ell^{E_i E_j, \text{fg}} C_\ell^{B_i B_j, \text{fg}} + C_\ell^{E_i B_j, \text{fg}} C_\ell^{B_i E_j, \text{fg}} \right] \\
& + \frac{s^2(4\beta)}{2c(4\alpha_i)c(4\alpha_j)} \left[\left(C_\ell^{E_i E_j, \Lambda\text{CDM}} \right)^2 + \left(C_\ell^{B_i B_j, \Lambda\text{CDM}} \right)^2 \right] \\
& + \frac{s(4\beta)c^2(2\alpha_i + 2\alpha_j)}{c(4\alpha_i)c(4\alpha_j)} \left[C_\ell^{E_i B_j, \text{fg}} + C_\ell^{B_i E_j, \text{fg}} \right] \left[C_\ell^{E_i E_j, \Lambda\text{CDM}} - C_\ell^{B_i B_j, \Lambda\text{CDM}} \right] \\
& + \frac{s^2(2\beta)}{c(4\alpha_i)c(4\alpha_j)} \left[C_\ell^{E_i E_j, \text{fg}} C_\ell^{E_i E_j, \Lambda\text{CDM}} + C_\ell^{B_i B_j, \text{fg}} C_\ell^{B_i B_j, \Lambda\text{CDM}} \right] \\
& + \frac{c^2(2\beta)}{c(4\alpha_i)c(4\alpha_j)} \left[C_\ell^{E_i E_j, \text{fg}} C_\ell^{B_i B_j, \Lambda\text{CDM}} + C_\ell^{B_i B_j, \text{fg}} C_\ell^{E_i E_j, \Lambda\text{CDM}} \right] \\
& + \frac{s^2(4\beta)}{c(4\alpha_i)c(4\alpha_j)} C_\ell^{E_i E_j, \Lambda\text{CDM}} C_\ell^{B_i B_j, \Lambda\text{CDM}}.
\end{aligned} \tag{D.3}$$

Adding all contributions, the total covariance in Eq. (C.1) is

$$\begin{aligned}
(2\ell + 1)f_{\text{sky}} \mathbf{C}_{ij\ell} = & \frac{1 + \mathcal{A}(\mathcal{A} - 2)}{c(4\alpha_i)c(4\alpha_j)} \left[C_\ell^{E_i E_j, \text{fg}} C_\ell^{B_i B_j, \text{fg}} + C_\ell^{E_i B_j, \text{fg}} C_\ell^{B_i E_j, \text{fg}} \right] \\
& + \frac{s(4\beta)c^2(2\alpha_i + 2\alpha_j)}{c(4\alpha_i)c(4\alpha_j)} \left[C_\ell^{E_i B_j, \text{fg}} + C_\ell^{B_i E_j, \text{fg}} \right] \left[C_\ell^{E_i E_j, \Lambda\text{CDM}} - C_\ell^{B_i B_j, \Lambda\text{CDM}} \right] \\
& + \frac{s^2(2\beta)}{c(4\alpha_i)c(4\alpha_j)} \left[C_\ell^{E_i E_j, \text{fg}} C_\ell^{E_i E_j, \Lambda\text{CDM}} + C_\ell^{B_i B_j, \text{fg}} C_\ell^{B_i B_j, \Lambda\text{CDM}} \right] \\
& + \frac{c^2(2\beta)}{c(4\alpha_i)c(4\alpha_j)} \left[C_\ell^{E_i E_j, \text{fg}} C_\ell^{B_i B_j, \Lambda\text{CDM}} + C_\ell^{B_i B_j, \text{fg}} C_\ell^{E_i E_j, \Lambda\text{CDM}} \right] \\
& + \frac{s^2(4\beta)}{c(4\alpha_i)c(4\alpha_j)} C_\ell^{E_i E_j, \Lambda\text{CDM}} C_\ell^{B_i B_j, \text{cmb}},
\end{aligned} \tag{D.4}$$

where the second term from Eq. (D.3) gets cancelled by the sum of $\mathbf{C}_{ij\ell}^{\text{CMB}}$ and $\mathbf{C}_{ij\ell}^{\text{CMB*o}}$ from Eqs. (C.5) and (C.6) as long as our theoretical model for the CMB angular power spectra is accurate enough. At high frequencies, Galactic foreground emission dominates over that of the CMB (especially at the largest scales), making the first term in Eq. (D.4) one of the main contributions to the total covariance. That term remains present if we do not account for the foreground EB correlation ($\mathcal{A} = 0$) in our likelihood, but gets cancelled when we use a good enough foreground template ($\mathcal{A} \approx 1$) to correct for it. This cancellation explains why including the foreground template leads to a reduction of the statistical uncertainties associated with our measurements.

It is also worth noting that $\mathbf{C}_{ij\ell}^{\text{fg*o}}$ is the term responsible for the reduction in the covariance matrix. Thus, the inclusion of foregrounds will indeed lead to an increase in statistical uncertainties if we ignored the correlations between template and data. The same happens with $\mathbf{C}_{ij\ell}^{\text{CMB}}$ and $\mathbf{C}_{ij\ell}^{\text{CMB*o}}$ correlations.

References

- [1] G. Gubitosi and F. Paci, *Constraints on cosmological birefringence energy dependence from CMB polarization data*, *J. Cosmology Astropart. Phys.* **2013** (2013) 020 [[1211.3321](#)].
- [2] D. J. E. Marsh, *Axion cosmology*, *Phys. Rep.* **643** (2016) 1 [[1510.07633](#)].
- [3] J. L. Feng, *Dark Matter Candidates from Particle Physics and Methods of Detection*, *ARA&A* **48** (2010) 495 [[1003.0904](#)].
- [4] J. Yoo and Y. Watanabe, *Theoretical Models of Dark Energy*, *Int. J. Mod. Phys. D* **21** (2012) 1230002 [[1212.4726](#)].
- [5] S. M. Carroll, G. B. Field and R. Jackiw, *Limits on a Lorentz- and parity-violating modification of electrodynamics*, *Phys. Rev. D* **41** (1990) 1231.
- [6] S. M. Carroll and G. B. Field, *Einstein equivalence principle and the polarization of radio galaxies*, *Phys. Rev. D* **43** (1991) 3789.
- [7] D. Harari and P. Sikivie, *Effects of a Nambu-Goldstone boson on the polarization of radio galaxies and the cosmic microwave background*, *Phys. Lett. B* **289** (1992) 67.
- [8] E. Komatsu, *New physics from the polarized light of the cosmic microwave background*, *Nat. Rev. Phys.* (2022) [[2202.13919](#)].
- [9] L. Campanelli, A. D. Dolgov, M. Giannotti and F. L. Villante, *Faraday Rotation of the Cosmic Microwave Background Polarization and Primordial Magnetic Field Properties*, *ApJ* **616** (2004) 1 [[astro-ph/0405420](#)].
- [10] K. Subramanian, *The origin, evolution and signatures of primordial magnetic fields*, *Rep. Prog. Phys.* **79** (2016) 076901 [[1504.02311](#)].
- [11] G. M. Shore, *Strong equivalence, Lorentz and CPT violation, anti-hydrogen spectroscopy and gamma-ray burst polarimetry*, *Nucl. Phys. B* **717** (2005) 86 [[hep-th/0409125](#)].
- [12] R. J. Gleiser and C. N. Kozameh, *Astrophysical limits on quantum gravity motivated birefringence*, *Phys. Rev. D* **64** (2001) 083007 [[gr-qc/0102093](#)].
- [13] J. R. Eskilt, *Frequency-dependent constraints on cosmic birefringence from the LFI and HFI Planck Data Release 4*, *A&A* **662** (2022) A10 [[2201.13347](#)].
- [14] A. Lue, L. Wang and M. Kamionkowski, *Cosmological Signature of New Parity-Violating Interactions*, *Phys. Rev. Lett.* **83** (1999) 1506 [[astro-ph/9812088](#)].
- [15] M. A. Fedderke, P. W. Graham and S. Rajendran, *Axion dark matter detection with CMB polarization*, *Phys. Rev. D* **100** (2019) 015040 [[1903.02666](#)].
- [16] H. Nakatsuka, T. Namikawa and E. Komatsu, *Is cosmic birefringence due to dark energy or dark matter? A tomographic approach*, *Phys. Rev. D* **105** (2022) 123509 [[2203.08560](#)].
- [17] B. Feng, M. Li, J.-Q. Xia, X. Chen and X. Zhang, *Searching for CPT Violation with Cosmic Microwave Background Data from WMAP and BOOMERANG*, *Phys. Rev. Lett.* **96** (2006) 221302 [[astro-ph/0601095](#)].
- [18] E. Y. S. Wu, P. Ade, J. Bock, M. Bowden, M. L. Brown, G. Cahill et al., *Parity Violation Constraints Using Cosmic Microwave Background Polarization Spectra from 2006 and 2007 Observations by the QUaD Polarimeter*, *Phys. Rev. Lett.* **102** (2009) 161302 [[0811.0618](#)].
- [19] G. Hinshaw, D. Larson, E. Komatsu, D. N. Spergel, C. L. Bennett, J. Dunkley et al., *Nine-year Wilkinson Microwave Anisotropy Probe (WMAP) Observations: Cosmological Parameter Results*, *ApJS* **208** (2013) 19 [[1212.5226](#)].
- [20] Planck Collaboration, *Planck intermediate results. XLIX. Parity-violation constraints from polarization data*, *A&A* **596** (2016) A110 [[1605.08633](#)].

- [21] T. Namikawa, Y. Guan, O. Darwish, B. D. Sherwin, S. Aiola, N. Battaglia et al., *Atacama Cosmology Telescope: Constraints on cosmic birefringence*, *Phys. Rev. D* **101** (2020) 083527 [[2001.10465](#)].
- [22] Polarbear Collaboration, *A Measurement of the Degree-scale CMB B-mode Angular Power Spectrum with POLARBEAR*, *ApJ* **897** (2020) 55 [[1910.02608](#)].
- [23] F. Bianchini, W. L. K. Wu, P. A. R. Ade, A. J. Anderson, J. E. Austermann, J. S. Avva et al., *Searching for anisotropic cosmic birefringence with polarization data from SPTpol*, *Phys. Rev. D* **102** (2020) 083504 [[2006.08061](#)].
- [24] S. K. Choi, M. Hasselfield, S.-P. P. Ho, B. Koopman, M. Lungu, M. H. Abitbol et al., *The Atacama Cosmology Telescope: a measurement of the Cosmic Microwave Background power spectra at 98 and 150 GHz*, *J. Cosmology Astropart. Phys.* **2020** (2020) 045 [[2007.07289](#)].
- [25] W. Hu, M. M. Hedman and M. Zaldarriaga, *Benchmark parameters for CMB polarization experiments*, *Phys. Rev. D* **67** (2003) 043004 [[astro-ph/0210096](#)].
- [26] M. Shimon, B. Keating, N. Ponthieu and E. Hivon, *CMB polarization systematics due to beam asymmetry: Impact on inflationary science*, *Phys. Rev. D* **77** (2008) 083003 [[0709.1513](#)].
- [27] N. J. Miller, M. Shimon and B. G. Keating, *CMB polarization systematics due to beam asymmetry: Impact on cosmological birefringence*, *Phys. Rev. D* **79** (2009) 103002 [[0903.1116](#)].
- [28] A. P. S. Yadav, M. Su and M. Zaldarriaga, *Primordial B-mode diagnostics and self-calibrating the CMB polarization*, *Phys. Rev. D* **81** (2010) 063512 [[0912.3532](#)].
- [29] B. G. Keating, M. Shimon and A. P. S. Yadav, *Self-calibration of Cosmic Microwave Background Polarization Experiments*, *ApJ* **762** (2013) L23 [[1211.5734](#)].
- [30] H. C. Chiang, P. A. R. Ade, D. Barkats, J. O. Battle, E. M. Bierman, J. J. Bock et al., *Measurement of Cosmic Microwave Background Polarization Power Spectra from Two Years of BICEP Data*, *ApJ* **711** (2010) 1123 [[0906.1181](#)].
- [31] S. Naess, M. Hasselfield, J. McMahon, M. D. Niemack, G. E. Addison, P. A. R. Ade et al., *The Atacama Cosmology Telescope: CMB polarization at $200 < l < 9000$* , *J. Cosmology Astropart. Phys.* **2014** (2014) 007 [[1405.5524](#)].
- [32] J. T. Sayre, C. L. Reichardt, J. W. Henning, P. A. R. Ade, A. J. Anderson, J. E. Austermann et al., *Measurements of B -mode polarization of the cosmic microwave background from 500 square degrees of SPTpol data*, *Phys. Rev. D* **101** (2020) 122003 [[1910.05748](#)].
- [33] Polarbear Collaboration, *A Measurement of the Degree-scale CMB B-mode Angular Power Spectrum with POLARBEAR*, *ApJ* **897** (2020) 55 [[1910.02608](#)].
- [34] P. Vielva, E. Martínez-González, F. J. Casas, T. Matsumura, S. Henrot-Versillé, E. Komatsu et al., *Polarization angle requirements for CMB B-mode experiments. Application to the LiteBIRD satellite*, *J. Cosmology Astropart. Phys.* **2022** (2022) 029 [[2202.01324](#)].
- [35] B. R. Johnson, C. J. Vourch, T. D. Drysdale, A. Kalman, S. Fujikawa, B. Keating et al., *A CubeSat for Calibrating Ground-Based and Sub-Orbital Millimeter-Wave Polarimeters (CalSat)*, *J. Astron. Instrum.* **4** (2015) 1550007 [[1505.07033](#)].
- [36] F. Nati, M. J. Devlin, M. Gerbino, B. R. Johnson, B. Keating, L. Pagano et al., *POLOCALC: A Novel Method to Measure the Absolute Polarization Orientation of the Cosmic Microwave Background*, *J. Astron. Instrum.* **6** (2017) 1740008 [[1704.02704](#)].
- [37] M. F. Navaroli, G. P. Teply, K. D. Crowley, J. P. Kaufman, N. B. Galitzki, K. S. Arnold et al., *Design and characterization of a ground-based absolute polarization calibrator for use with polarization sensitive CMB experiments*, in *Millimeter, Submillimeter, and Far-Infrared Detectors and Instrumentation for Astronomy IX*, J. Zmuidzinas and J.-R. Gao, eds., vol. 10708 of Proc. SPIE, p. 107082A, July, 2018, DOI [[1809.02111](#)].

- [38] F. J. Casas, E. Martínez-González, J. Bermejo-Ballesteros, S. García, J. Cubas, P. Vielva et al., *L2-CalSat: A Calibration Satellite for Ultra-Sensitive CMB Polarization Space Missions*, *Sensors* **21** (2021) 3361.
- [39] LiteBIRD Collaboration, *Probing Cosmic Inflation with the LiteBIRD Cosmic Microwave Background Polarization Survey*, *PTEP ptac150* (2022) [2202.02773].
- [40] P. Ade, J. Aguirre, Z. Ahmed, S. Aiola, A. Ali, D. Alonso et al., *The Simons Observatory: science goals and forecasts*, *J. Cosmology Astropart. Phys.* **2019** (2019) 056 [1808.07445].
- [41] K. Abazajian, G. Addison, P. Adshead, Z. Ahmed, S. W. Allen, D. Alonso et al., *CMB-S4 Science Case, Reference Design, and Project Plan*, *arXiv e-prints* (2019) arXiv:1907.04473 [1907.04473].
- [42] Y. Minami, H. Ochi, K. Ichiki, N. Katayama, E. Komatsu and T. Matsumura, *Simultaneous determination of the cosmic birefringence and miscalibrated polarization angles from cmb experiments*, *PTEP* **2019** (2019) 083E02 [1904.12440].
- [43] Y. Minami, *Determination of miscalibrated polarization angles from observed cosmic microwave background and foreground EB power spectra: Application to partial-sky observation*, *PTEP* **2020** (2020) 063E01 [2002.03572].
- [44] Y. Minami and E. Komatsu, *Simultaneous determination of the cosmic birefringence and miscalibrated polarization angles II: Including cross-frequency spectra*, *PTEP* **2020** (2020) 103E02 [2006.15982].
- [45] N. Krachmalnicoff, T. Matsumura, E. de la Hoz, S. Basak, A. Gruppuso, Y. Minami et al., *In-flight polarization angle calibration for LiteBIRD: blind challenge and cosmological implications*, *J. Cosmology Astropart. Phys.* **2022** (2022) 039 [2111.09140].
- [46] Y. Minami and E. Komatsu, *New Extraction of the Cosmic Birefringence from the Planck 2018 Polarization Data*, *Phys. Rev. Lett.* **125** (2020) 221301 [2011.11254].
- [47] Planck Collaboration, *Planck 2018 results. III. High Frequency Instrument data processing and frequency maps*, *A&A* **641** (2020) A3 [1807.06207].
- [48] Planck Collaboration, *Planck intermediate results. LVII. Joint Planck LFI and HFI data processing*, *A&A* **643** (2020) A42 [2007.04997].
- [49] P. Diego-Palazuelos, J. R. Eskilt, Y. Minami, M. Tristram, R. M. Sullivan, A. J. Banday et al., *Cosmic Birefringence from the Planck Data Release 4*, *Phys. Rev. Lett.* **128** (2022) 091302 [2201.07682].
- [50] Planck Collaboration, *Planck 2018 results. XI. Polarized dust foregrounds*, *A&A* **641** (2020) A11 [1801.04945].
- [51] F. A. Martire, R. B. Barreiro and E. Martínez-González, *Characterization of the polarized synchrotron emission from Planck and WMAP data*, *J. Cosmology Astropart. Phys.* **2022** (2022) 003 [2110.12803].
- [52] K. M. Huffenberger, A. Rotti and D. C. Collins, *The Power Spectra of Polarized, Dusty Filaments*, *ApJ* **899** (2020) 31 [1906.10052].
- [53] S. E. Clark, C.-G. Kim, J. C. Hill and B. S. Hensley, *The origin of parity violation in polarized dust emission and implications for cosmic birefringence*, *ApJ* **919** (2021) 53 [2105.00120].
- [54] A. J. Cukierman, S. E. Clark and G. Halal, *Magnetic Misalignment of Interstellar Dust Filaments*, *arXiv e-prints* (2022) arXiv:2208.07382 [2208.07382].
- [55] J. Jewell, S. Levin and C. H. Anderson, *Application of Monte Carlo Algorithms to the Bayesian Analysis of the Cosmic Microwave Background*, *ApJ* **609** (2004) 1 [astro-ph/0209560].

- [56] B. D. Wandelt, D. L. Larson and A. Lakshminarayanan, *Global, exact cosmic microwave background data analysis using Gibbs sampling*, *Phys. Rev. D* **70** (2004) 083511 [[astro-ph/0310080](#)].
- [57] H. K. Eriksen, I. J. O’Dwyer, J. B. Jewell, B. D. Wandelt, D. L. Larson, K. M. Górski et al., *Power Spectrum Estimation from High-Resolution Maps by Gibbs Sampling*, *ApJS* **155** (2004) 227 [[astro-ph/0407028](#)].
- [58] H. K. Eriksen, J. B. Jewell, C. Dickinson, A. J. Banday, K. M. Górski and C. R. Lawrence, *Joint Bayesian Component Separation and CMB Power Spectrum Estimation*, *ApJ* **676** (2008) 10 [[0709.1058](#)].
- [59] J. R. Eskilt and E. Komatsu, *Improved constraints on cosmic birefringence from the WMAP and Planck cosmic microwave background polarization data*, *Phys. Rev. D* **106** (2022) 063503 [[2205.13962](#)].
- [60] E. de la Hoz, P. Diego-Palazuelos, E. Martínez-González, P. Vielva, R. B. Barreiro and J. D. Bilbao-Ahedo, *Determination of polarization angles in CMB experiments and application to CMB component separation analyses*, *J. Cosmology Astropart. Phys.* **2022** (2022) 032 [[2110.14328](#)].
- [61] S. Saito, K. Ichiki and A. Taruya, *Probing polarization states of primordial gravitational waves with cosmic microwave background anisotropies*, *J. Cosmology Astropart. Phys.* **2007** (2007) 002 [[0705.3701](#)].
- [62] T. Fujita, Y. Minami, M. Shiraishi and S. Yokoyama, *Can primordial parity violation explain the observed cosmic birefringence?*, *arXiv e-prints* (2022) arXiv:2208.08101 [[2208.08101](#)].
- [63] M.-A. Watanabe, S. Kanno and J. Soda, *Imprints of the anisotropic inflation on the cosmic microwave background*, *MNRAS* **412** (2011) L83 [[1011.3604](#)].
- [64] Planck Collaboration, *Planck 2015 results. X. Diffuse component separation: Foreground maps*, *A&A* **594** (2016) A10 [[1502.01588](#)].
- [65] Planck Collaboration, *Planck 2018 results. IV. Diffuse component separation*, *A&A* **641** (2020) A4 [[1807.06208](#)].
- [66] K. Tassis and V. Pavlidou, *Searching for inflationary B modes: can dust emission properties be extrapolated from 350 GHz to 150 GHz?*, *MNRAS* **451** (2015) L90 [[1410.8136](#)].
- [67] Planck Collaboration, *Planck intermediate results. L. Evidence of spatial variation of the polarized thermal dust spectral energy distribution and implications for CMB B-mode analysis*, *A&A* **599** (2017) A51 [[1606.07335](#)].
- [68] L. Vacher, J. Chluba, J. Aumont, A. Rotti and L. Montier, *High precision modeling of polarized signals: moment expansion method generalized to spin-2 fields*, Accepted for publication in *A&A* (2022) [[2205.01049](#)].
- [69] V. Pelgrims, S. E. Clark, B. S. Hensley, G. V. Panopoulou, V. Pavlidou, K. Tassis et al., *Evidence for line-of-sight frequency decorrelation of polarized dust emission in Planck data*, *A&A* **647** (2021) A16 [[2101.09291](#)].
- [70] A. Ritacco, F. Boulanger, V. Guillet, J.-M. Delouis, J.-L. Puget, J. Aumont et al., *Dust polarization spectral dependence from Planck HFI data. Turning point on CMB polarization foregrounds modelling*, *arXiv e-prints* (2022) arXiv:2206.07671 [[2206.07671](#)].
- [71] L. Vacher, J. Aumont, F. Boulanger, L. Montier, V. Guillet, A. Ritacco et al., *Frequency dependence of the thermal dust E/B ratio and EB correlation: insights from the spin-moment expansion*, *arXiv e-prints* (2022) arXiv:2210.14768 [[2210.14768](#)].
- [72] Planck Collaboration, *Planck 2015 results. XII. Full focal plane simulations*, *A&A* **594** (2016) A12 [[1509.06348](#)].

- [73] E. Hivon, S. Mottet and N. Ponthieu, *QuickPol: Fast calculation of effective beam matrices for CMB polarization*, *A&A* **598** (2017) A25 [[1608.08833](#)].
- [74] E. Hivon, K. M. Górski, C. B. Netterfield, B. P. Crill, S. Prunet and F. Hansen, *MASTER of the Cosmic Microwave Background Anisotropy Power Spectrum: A Fast Method for Statistical Analysis of Large and Complex Cosmic Microwave Background Data Sets*, *ApJ* **567** (2002) 2 [[astro-ph/0105302](#)].
- [75] A. Challinor and G. Chon, *Error analysis of quadratic power spectrum estimates for cosmic microwave background polarization: sampling covariance*, *MNRAS* **360** (2005) 509 [[astro-ph/0410097](#)].
- [76] D. Alonso, J. Sanchez, A. Slosar and LSST Dark Energy Science Collaboration, *A unified pseudo- C_ℓ framework*, *MNRAS* **484** (2019) 4127 [[1809.09603](#)].
- [77] L. McBride, P. Bull and B. S. Hensley, *Characterizing line-of-sight variability of polarized dust emission with future CMB experiments*, *arXiv e-prints* (2022) arXiv:2207.14213 [[2207.14213](#)].
- [78] L. Vacher, J. Aumont, L. Montier, S. Azzoni, F. Boulanger and M. Remazeilles, *Moment expansion of polarized dust SED: A new path towards capturing the CMB B-modes with LiteBIRD*, *A&A* **660** (2022) A111 [[2111.07742](#)].
- [79] Planck Collaboration, *Planck 2018 results. I. Overview and the cosmological legacy of Planck*, *A&A* **641** (2020) A1 [[1807.06205](#)].
- [80] E. de la Hoz, P. Vielva, R. B. Barreiro and E. Martínez-González, *On the detection of CMB B-modes from ground at low frequency*, *J. Cosmology Astropart. Phys.* **2020** (2020) 006 [[2002.12206](#)].
- [81] A. Lewis and A. Challinor, *CAMB: Code for Anisotropies in the Microwave Background*, Feb., 2011.
- [82] K. M. Górski, E. Hivon, A. J. Banday, B. D. Wandelt, F. K. Hansen, M. Reinecke et al., *HEALPix: A Framework for High-Resolution Discretization and Fast Analysis of Data Distributed on the Sphere*, *ApJ* **622** (2005) 759 [[astro-ph/0409513](#)].
- [83] D. Foreman-Mackey, D. W. Hogg, D. Lang and J. Goodman, *emcee: The MCMC Hammer*, *PASP* **125** (2013) 306 [[1202.3665](#)].
- [84] D. Foreman-Mackey, *corner.py: Scatterplot matrices in Python*, *The Journal of Open Source Software* **1** (2016) 24.
- [85] J. D. Hunter, *Matplotlib: A 2D Graphics Environment*, *Comput. Sci. Eng.* **9** (2007) 90.
- [86] C. R. Harris, K. J. Millman, S. J. van der Walt, R. Gommers, P. Virtanen, D. Cournapeau et al., *Array programming with NumPy*, *Nature* **585** (2020) 357 [[2006.10256](#)].